Quaternary Science Reviews 171 (2017) 119–135

Contents lists available at ScienceDirect

Quaternary Science Reviews

journal homepage: www.elsevier.com/locate/quascirev

Millennial-scale fluctuations in Saharan dust supply across the decline of the African Humid Period

Christoph Zielhofer [a, *], Hans von Suchodoletz [a], William J. Fletcher [b], Birgit Schneider [a], Elisabeth Dietze [c], Michael Schlegel [a], Kerstin Schepanski [d], Bernhard Weninger [e], Steffen Mischke [f], Abdeslam Mikdad [g]

[a] Chair of Physical Geography, Leipzig University, Leipzig, Germany
[b] Department of Geography, School of Environment, Education and Development, University of Manchester, Manchester, United Kingdom
[c] GFZ German Research Centre for Geosciences, Section 5.2, Climate Dynamics and Landscape Evolution, Potsdam, Germany
[d] TROPOS – Leibniz Institute for Tropospheric Research, Leipzig, Germany
[e] Institute of Pre- and Early History, Cologne University, Cologne, Germany
[f] Faculty of Earth Sciences, University of Iceland, Reykjavík, Iceland
[g] Institut National des Sciences de l'Archéologie et du Patrimoine, Rabat, Morocco

ARTICLE INFO

Article history:
Received 21 February 2017
Received in revised form
10 July 2017
Accepted 11 July 2017
Available online 17 July 2017

Keywords:
Holocene
Palaeolimnology
Palaeoclimatology
North Atlantic
Western Mediterranean
Morocco
Sahara
Dust record
Inorganic geochemistry

ABSTRACT

The Sahara is the world's largest dust source with significant impacts on *trans*-Atlantic terrestrial and large-scale marine ecosystems. Contested views about a gradual or abrupt onset of Saharan aridity at the end of the African Humid Period dominate the current scientific debate about the Holocene Saharan desiccation. In this study, we present a 19.63 m sediment core sequence from Lake Sidi Ali (Middle Atlas, Morocco) at the North African desert margin. We reconstruct the interaction between Saharan dust supply and Western Mediterranean hydro-climatic variability during the last 12,000 yr based on analyses of lithogenic grain-sizes, XRF geochemistry and stable isotopes of ostracod shells. A robust chronological model based on AMS ^{14}C dated pollen concentrates supports our multi-proxy study. At orbital-scale there is an overall increase in southern dust supply from the Early Holocene to the Late Holocene, but our Northern Saharan dust record indicates that a gradual Saharan desiccation was interrupted by multiple abrupt dust increases before the 'southern dust mode' was finally established at 4.7 cal ka BP. The Sidi Ali record features millennial peaks in Saharan dust increase at about 11.1, 10.2, 9.4, 8.2, 7.3, 6.6, 6.0, and 5.0 cal ka BP. Early Holocene Saharan dust peaks coincide with Western Mediterranean winter rain minima and North Atlantic cooling events. In contrast, Late Holocene dust peaks correspond mostly with prevailing positive phases of the North Atlantic Oscillation. By comparing with other North African records, we suggest that increases in Northern Saharan dust supply do not solely indicate sub-regional to regional aridity in Mediterranean Northwest Africa but might reflect aridity at a *trans*-Saharan scale. In particular, our findings support major bimillennial phases of *trans*-Saharan aridity at 10.2, 8.2, 6.0 and 4.2 cal ka BP. These phases coincide with North Atlantic cooling and a weak African monsoon.

1. Introduction

The Sahara is the world's largest dust source (Ginoux et al., 2012; Goudie and Middleton, 2001) with significant impacts on *trans*-Atlantic terrestrial environments (Bristow et al., 2010; Muhs et al., 1990; Prospero and Lamb, 2003), Canary soil properties (Suchodoletz et al., 2013), Mediterranean forests (Avila et al., 1998) and large-scale marine ecosystems (Jickells et al., 2005; Mahowald et al., 2010). Remote Saharan dust influences the earth's radiation budget (Kaufman et al., 2002) and tropical North Atlantic ocean-atmosphere temperature variability (Evan et al., 2011) that might even attenuate Hurricane activity (Evan et al., 2016).

The intensity of Saharan dust mobilisation varies over different time-scales (Albani et al., 2015; Bout-Roumazeilles et al., 2013; Ehrmann et al., 2017; Goudie, 2009; Jullien et al., 2007; Kuhlmann et al., 2004). In the range of instrumental records and historical reanalyses, Sahelian droughts (Evan et al., 2016; Goudie and Middleton, 2001) and positive phases of the North Atlantic

* Corresponding author.
E-mail address: zielhofer@uni-leipzig.de (C. Zielhofer).

http://dx.doi.org/10.1016/j.quascirev.2017.07.010

Oscillation (Chiapello and Moulin, 2002; Ginoux et al., 2004; Mahowald et al., 2003; Moulin et al., 1997) are considered the two most important climatic drivers for accelerating Saharan dust mobilisation and its long-range dispersal. However, regarding the entire Holocene, a much longer time period that covers the last 11,700 years, the forcing mechanisms and frequencies of Saharan dust mobilisation remain controversial (deMenocal et al., 2000a; Kröpelin et al., 2008; Longman et al., 2017).

The orbital-scale increase in northern hemispherical summer insolation led to the large-scale expansion of the tropical rain belt and to the onset of the African Humid Period at about 14.8 cal ka BP (Shanahan et al., 2015). One of the most prominent ecological changes during the Holocene was the end of the African Humid Period with the transition from the 'green' Sahara towards the hyperarid desert today. With respect to different North African investigation sites, this mid-Holocene desiccation of the Sahara took place between 7 and 3 cal ka BP (Shanahan et al., 2015). Generally, an earlier onset of aridity can be observed at the northern Saharan margin at about 7 cal ka BP in contrast to relatively humid conditions that persisted at the southern Saharan margin until 3 cal ka BP (Shanahan et al., 2015). Alongside declining summer insolation, powerful vegetation-climate feedbacks may be implicated in the end of the African Humid Period (Renssen et al., 2006).

The mid-Holocene desiccation of the Sahara stopped the natural potential of North African geological archives for recording the Holocene environmental history of the world's largest desert. To date, there is only one terrestrial record from the Sahara itself that covers the last 6000 years. The Lake Yoa record (Fig. 1) documents a continuous and gradual desiccation from the Mid-Holocene until today (Kröpelin et al., 2008). In contrast, marine core ODP 658C (deMenocal et al., 2000a, Fig. 1) taken off the coast of NW-Africa documents an abrupt mid-Holocene onset of increased Saharan dust supply at ~5.0 cal ka BP. This abrupt shift is also visible with some uncertainty in marine cores of the tropical Western and subtropical North Atlantic (Williams et al., 2016). Modelling approaches indicate abrupt vegetation collapses as a response to gradual decreases in summer insolation and precipitation in the Western Sahara at that time (deMenocal et al., 2000a; Liu et al., 2007). However, due to the missing multi-proxy evidence from terrestrial archives in the Western Sahara itself, there are gaps in the knowledge about timing and extent of probable cross-Saharan desiccation during the Holocene. This leads to the controversial views about a gradual (Kröpelin et al., 2008; Kuper and Kröpelin, 2006; Shanahan et al., 2015) or abrupt (deMenocal et al., 2000a; Tierney et al., 2017) onset of Saharan desiccation at the end of the African Humid Period that dominate the current scientific debate (Egerer et al., 2016).

A 19.63 m long core from Lake Sidi Ali (Moroccan Middle Atlas) within the intercalation zone of North Atlantic and Saharan air mass trajectories (Figs. 1 and 2) provided for the first time a robustly dated (Fletcher et al., 2017) multi-proxy reconstruction of hydro-climatic variability at the North African desert margin for the last 12,000 years (Zielhofer et al., 2017). In the new study presented here, we aim to reconstruct from the same core the Holocene variability of Saharan dust supply. Selected siliciclastic element ratios from terrestrial sampling sites alongside a transect at the North African desert margin are used for the first time as geochemical tracers and compared with those ratios from the Sidi Ali core to gain information about shifting dust provenance. We compare shifts in dust provenance with changes in aeolian grain size. Finally, we evaluate probable synchronicities between Saharan dust mobilisation and the North Atlantic hydro-climate during the Holocene.

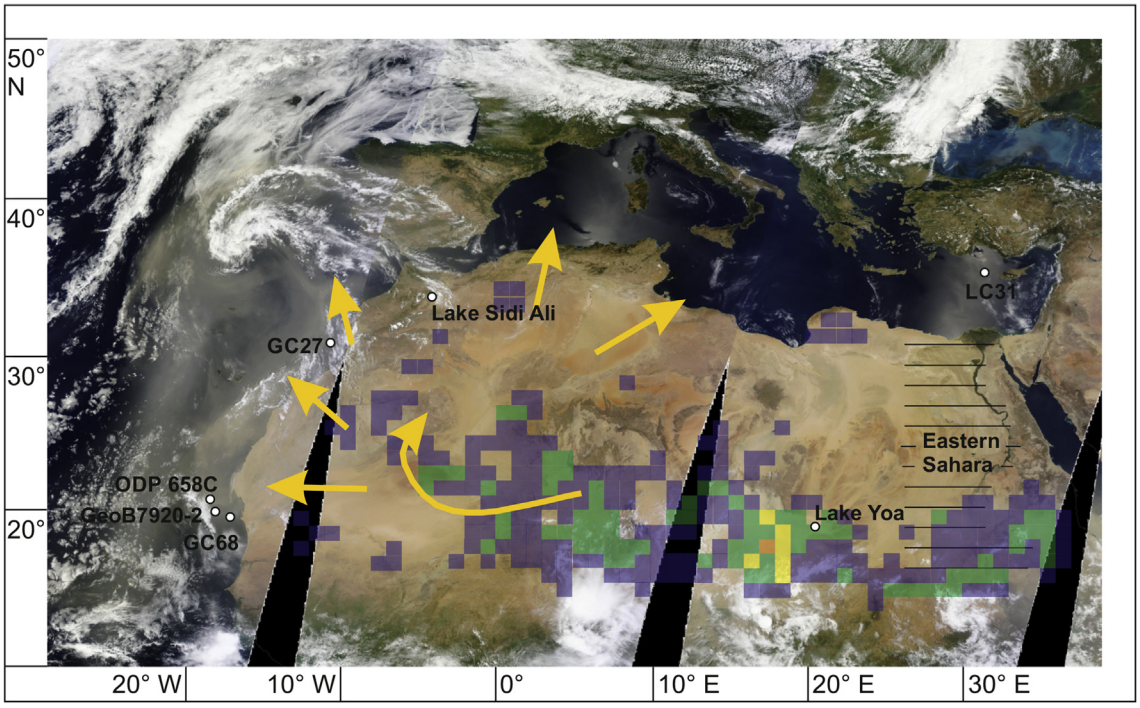

Fig. 1. Overview satellite image with major circum-Saharan sites discussed in this manuscript, showing Lake Sidi Ali (this study), Eastern Saharan geoarcheological record (horizontal lines, Kuper and Kröpelin, 2006), Central Saharan Lake Yoa (Ounianga Kebir, Kröpelin et al., 2008), off Morocco GC27 Site (Tierney et al., 2017), off Mauretania ODP Site 658C (deMenocal et al., 2000a, 2000b), off Mauretania GeoB7920-2 core (Tjallingii et al., 2008), off Mauretania GC68 Site (Tierney et al., 2017), and Eastern Mediterranean LC31 marine core (Schmiedl et al., 2010). Blue, green, yellow and orange backgrounds indicate moderate to major dust production areas based on MSG SEVIRI infrared dust index (Schepanski et al., 2009). Yellow arrows indicate major Saharan dust trajectories towards the subtropical North Atlantic and the Mediterranean Basin (Ashpole and Washington, 2013; Schepanski et al., 2016). The composed satellite images were obtained on 26 June 2012 by MODIS (Moderate Resolution Imaging Spectroradiometer) flying aboard NASA's Terra satellite (NASA, 2016). (For interpretation of the references to colour in this figure legend, the reader is referred to the web version of this article.)

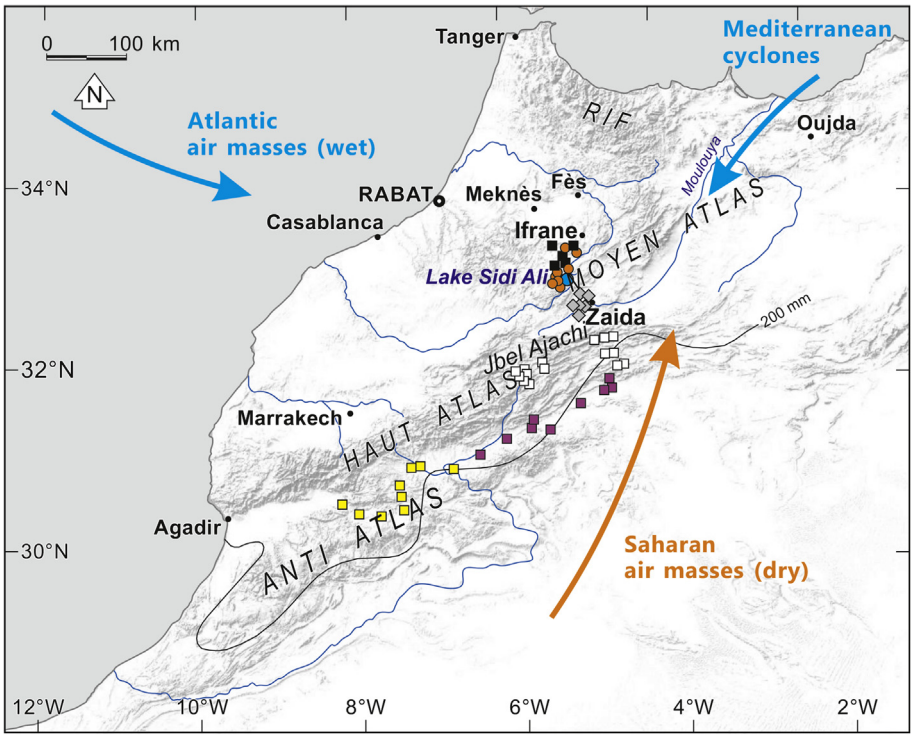

Fig. 2. Lake Sidi Ali in the Middle Atlas (*Moyen Atlas*) close to the Northern Saharan desert margin modified from Zielhofer et al. (2017). Arrows show the potential influence of North Atlantic, Mediterranean and Saharan air masses on the Holocene Sidi Ali lake record. Black squares show surface sampling sites from Northern Middle Atlas volcanic deposits, orange circles from the Middle Atlas (*Moyen Atlas*), grey diamonds from the Upper Moulouya Basin, white squares from the High Atlas (*Haut Atlas*), purple squares from the pre-Saharan Basin, and yellow squares from the Anti-Atlas foothills. (For interpretation of the references to colour in this figure legend, the reader is referred to the web version of this article.)

Our study covers the transition from the 'green' Sahara during the African Humid Period toward the present-day hyper-arid desert. In the face of contrasting inferences from the available Saharan dust records of either an abrupt (Egerer et al., 2016; deMenocal et al., 2000a) or a gradual (Kröpelin et al., 2008) ecosystem shift from a 'green' Sahara towards a hyper-arid desert at the end of the African Humid Period, the Sidi Ali record should provide valuable new data for advancing this ongoing scientific debate. In particular, the co-registration of Saharan dust and North-Atlantic hydro-climatic proxies in the same core without relative age uncertainties allows for the reconstruction of teleconnections between Saharan and North Atlantic air masses during the Holocene. Furthermore, Lake Sidi Ali may be a key site for reconstructing large-scale atmospheric coupling of the Atlantic, Mediterranean and Saharan climatic sub-systems in the northern Hemisphere. The Sidi Ali hydro-climatic record (Zielhofer et al., 2017) indicates that precipitation in the Western Mediterranean is characterised by a significant millennial-scale variability with winter rain minima in phase with North Atlantic cooling events during the Early Holocene, and by a multi-centennial-scale variability with winter rain minima corresponding generally with positive NAO-like stages during the Late Holocene. Here, we aim to explore probable synchronicities between outer-tropical North Atlantic and tropical monsoonal air masses, and to determine whether Holocene arid phases at the northern Saharan desert margin might relate more widely to *trans*-Saharan and sub-Saharan aridity.

2. Geographical setting

The geographical position of the karstic Lake Sidi Ali in the Middle Atlas (N 33° 03′, E 5° 00', 2080 m a.s.l.) is within the North Saharan mountainous desert margin of Morocco between the sub-humid Mediterranean climate in the North and the arid Saharan climate in the South (Fig. 2 and Supplementary Online Material). The mean annual precipitation at Lake Sidi Ali is 430 mm with a mean annual temperature of 10.3 °C (mean JJA maximum, 32.5 °C; mean DJF minimum, -8.4 °C) and a dry season lasting from June to September (Supplementary Online Material). The surrounding forest vegetation consists of evergreen oak (*Quercus rotundifolia*) and Atlantic cedar (*Cedrus atlantica*) but is strongly degraded due to overgrazing. The lake lies within a small catchment of approx. 14 km^2 and has a varying surface between 2.0 and 2.8 km^2 (Sayad et al., 2011).

The petrography in the Lake Sidi Ali area includes Plio-Quaternary volcanic ashes and lapilli exclusively in the northern sector (Saadi et al., 1985). In contrast, the petrography of the wider Middle Atlas and the adjacent High Atlas (Djebel Ajachi, 3747 m a.s.l.) further south is dominated by ubiquitous Lower and Middle Jurassic dolomites and limestones and Triassic continental series (Piqué, 2001; Schlüter, 2008). Therefore, the petrographic setting should provide ideal conditions for a geochemical provenance analysis of siliciclastic components into the lake.

3. Previously published data

3.1. Lake Sidi Ali core recovery and chronology

At the deepest part of Lake Sidi Ali we conducted a drilling campaign in September 2012. A 19.56 m sequence from a single borehole was recovered (Supplementary Online Material) using a UWITEC piston corer. The sediments comprised horizontally bedded, faintly laminated, organic silts without any hiatus or major sedimentological shifts, and contained aquatic macrofossils including aquatic plant fragments (*Potamogeton*), ostracods and

fish bones. Full details of the surveys, coring and sedimentological analyses are given in Zielhofer et al. (2017). A Bayesian age model is based on 26 AMS ^{14}C dates on pollen concentrates and terrestrial plant remains and ^{210}Pb and ^{137}Cs radiometric dating (Fletcher et al., 2017). The age model reveals a robust chronology for the Sidi Ali core, which provides a continuous record for the last 12,000 years (Fig. 3).

3.2. Lake Sidi Ali stable isotope record

A stable oxygen isotope (δ^{18}O) record was developed on benthic ostracods (n = 118) with a mean annual resolution of ~100 years (Zielhofer et al., 2017). In this context, enrichment in δ^{18}O is interpreted as a signal of reduced Atlantic winter rainfall to the lake system.

3.3. Lake Sidi Ali XRF record

A first set of robust XRF (Spectro: K, Ti, Fe, Ca, S) and XRF scanning (ITRAX: Ca) data from Sidi Ali core was already presented in an earlier paper (Zielhofer et al., 2017) with a major focus on lake internal productivity and lake level changes (S/Fe and Ca record) and a minor focus on catchment soil erosion (K, Fe and Ti record). In contrast, the analytical data sets that are shown for the first time in the present publication will focus on the XRF-based reconstruction of siliciclastic provenances and dust mobilisation.

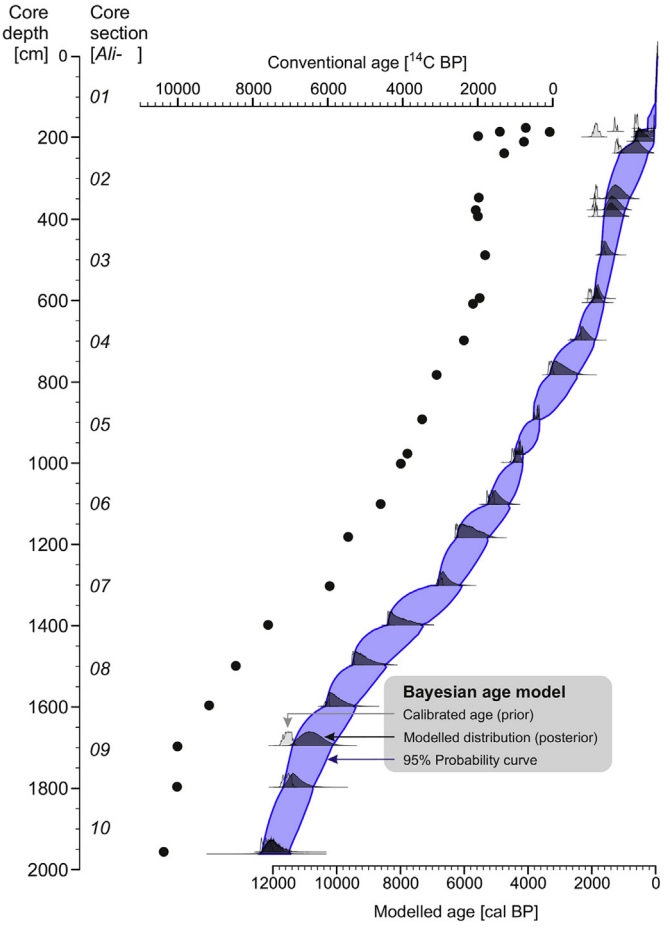

Fig. 3. Bayesian age model of the Sidi Ali core (Fletcher et al., 2017): the black dots show conventional ^{14}C ages [BP]. The light greyish curves show ^{14}C calibrated ages (prior). The dark greyish curves show modelled age distributions (posterior). The light purple area show the 95% probability distribution. Calibration (2 sigma) of the conventional radiocarbon ages was performed using intcal13.14c. (For interpretation of the references to colour in this figure legend, the reader is referred to the web version of this article.)

4. Material and methods

4.1. Modern dust concentrations

Dust concentrations at Lake Sidi Ali are determined using archived dust concentrations (CONC_DUST) of BSC-DREAM8b (Barcelona Supercomputing Center's Dust REgional Atmospheric Model) v2.0 for the period between 1st January 2006 and 31st December 2014. The model predicts dust concentrations in arid and semi-arid regions by solving Euler-type partial differential non-linear equations based on (i) NCEP/ETA data describing atmospheric processes, and (ii) a model that predicts dust production and concentration based on global US Geological Survey and FAO data including information about soil and vegetation type, soil moisture and atmospheric turbulence. The meteorological fields are initialized every 24 h, while the boundary conditions are updated every 6 h (Basart et al., 2012). The temporal resolution of the dust concentration data is 1 h, the horizontal resolution 0,33° x 0,33°, and the vertical resolution in 24 layers between 0 and 15 km (Basart et al., 2012). In this study, we aggregate daily dust concentrations at 12.00 UTC for 2100 m a.s.l. into monthly data whereof mean and standard deviation are shown. These data are coupled with wind directions derived from the NOAA-HYSPLIT (Hybrid Single-Particle Lagrangian Integrated Trajectory) model for the year 2007, a Lagrange/Eulerian hybrid model that works with a spatial resolution of 1° × 1°. Monthly dust concentrations of 2007 show the best fit with the average of 2006–2014 ($R^2 = 0.96$) so that this year should represent a typical one for recent dust input. Backward trajectories of the last 24 h are calculated for Sidi Ali at 2100 m a.s.l. for every day at 12.00 UTC, and wind directions are divided into eight directions (N, NE, E, SE, S, SW, W, NW).

4.2. Geochemical provenance parameters

We conduct a northeast-southwest transect of surface sediment sampling sites from the Middle Atlas into the pre-Saharan Basin in order to develop a gradient of Sidi Ali siliciclastic provenances (Fig. 2 and Supplementary Online Material). We use surface bulk samples from the volcanic (ashes and lapilli) and non-volcanic sectors of the Middle Atlas, the Upper Moulouya Basin, the High Atlas, the pre-Saharan depression and the Anti-Atlas foothills (Saadi et al., 1985) for catchment-, regional- and supra-regional-scale XRF provenance analyses.

Bulk materials from surface samples and Sidi Ali cores are analysed with a Spectro Xepos X-ray fluorescence (XRF) device. The XRF sampling of the core sequence is every 20 cm, which corresponds with a mean chronological resolution of ~120 years. For XRF sample preparation air-dried bulk sediment (4 g) is sieved (2 mm). Subsequently a homogenization of the sample is undertaken with a Planetary Ball Mill PM 200. Pressed pellets are prepared using a Vaneox press at 20 t for 2 min. Measurements are conducted in a He atmosphere. We conduct a second XRF record from the same core to attain totally a higher sampling density of 10 cm corresponding with a mean chronological resolution of ~60 years. Both XRF records provide plausible quantitative data for most elements (e.g. K, Ti). However, there is one exception. Due to a slight quantitative scattering between the Al values of the first and second XRF record, we only use the data for atomically light Al obtained at the primary mean resolution of ~120 years. The scattering is particularly visible within the element ratio records (Supplementary Online Material, e.g. Fig. S1m).

We calculate a variety of siliciclastic element ratios for the

reconstruction of local and remote provenance signals. According to Wehausen and Brumsack (2000), who successfully used a high Ti/Al ratio as a proxy for volcanic provenances, we try to detect siliciclastic element ratios that show significant geo-chemical signals of Middle Atlas volcanic ashes and lapilli. Additionally, we test element ratios that were suggested or published in former North African dust provenance studies (Castillo et al., 2008; Engelbrecht et al., 2014; Moreno et al., 2006; Muhs et al., 1990; Rodrigo-Gámiz et al., 2014; Scheuvens et al., 2013; Wu et al., 2016). However, we discard many element ratios that were applied in former Saharan dust provenance studies because many elements (e.g. Ca, Sr, P, S, Fe, Mn) will be easily affected by lake-internal precipitation and redox processes. Finally, we identify Cr/Al, Ni/Al, Ti/Al, K/Ti, Ti/Th and Ti/Zr ratios (Supplementary Online Material) as probable geochemical provenance signals.

Regarding the K/Ti ratio as a probable geochemical provenance signal, we conduct a XRF core scanning record in a stratigraphical resolution of 1 mm (Supplementary Online Material). Split core halves are analysed with an ITRAX XRF core scanner to obtain a high-resolution K and Ti record (Croudace et al., 2006). The K and Ti intensities obtained by the XRF core scanner are calibrated using discrete XRF Spectro samples (n = 198) and a multivariate log-ratio calibration model (Weltje et al., 2015).

4.3. Detrital sedimentation rate

Elements that are related predominantly to detrital sediment components (Kylander et al., 2011) were used to calculate a proxy for the Lake Sidi Ali detrital sedimentation rate. The proportions of major detrital elements (Al, Ti, Mg, K, and Na) were expressed as oxides and summed to create a proxy for the detrital content within the core. Si, Fe and Ca were not considered because SiO_2, Fe-Oxides and particularly $CaCO_3$ are not only constrained to detrital minerals but also to lake internal processes (biogenic SiO_2, Fe redox processes and $CaCO_3$ precipitation). Our proxy for the detrital sedimentation rate [cm/a] is the result of the total sedimentation rate multiplied by the relative detrital sum of Al_2O_3, TiO_2, MgO, K_2O and Na_2O contents.

4.4. Grain size analyses and end-member modelling

Sediment grain sizes of 124 core samples are determined using a Malvern Mastersizer laser diffraction particle size analyser. The grain-size samples derive from the same depths as the XRF Spectro samples. Dry bulk samples of 0.25 g are pre-treated with 5–10 mL of 10% HCl to eliminate carbonates and with 5 mL of 30% H_2O_2 to eliminate organic matter. The remaining sediment is dispersed using 5 mL 0.4 N sodium pyrophosphate solution ($Na_4P_2O_7$). A robust end-member modelling analysis (EMMA) (Dietze et al., 2012, 2014) that applies principles of eigenspace analysis and different scaling procedures to all non-zero grain size classes in all 124 samples is calculated using the open-source software R and the package EMMAgeo version 0.9.0 (Dietze and Dietze, 2013). Hence, end-member loadings can be interpreted in terms of individual grain-size subpopulations and scores representing the contribution of these subpopulations to the samples.

4.5. Data transformation and principal component analysis

Geochemical data are commonly expressed as relative concentrations and represent the abundance of certain elements as fractions of a given unit value (e.g. ppm, percentage, g/kg, etc.). Consequently, element concentrations do not vary independently due to the closed-sum constraint, but all variables are intrinsically correlated. This constraint affects the covariance and correlation matrices of compositional data and might greatly bias statistical results. A solution to this problem is provided by log-ratio transformation of compositional data, which is required for robust multivariate statistical results. Prior to the principal component analyses, all core sediment data (element and grain size end-member ratios) are expressed as logarithms of ratios of the initial data and subsequently normalized (z-score) to minimize the effects of different data units (Aitchison, 1982, 1999). For the total core record we use a principal component analysis (PCA) as a tool for multivariate statistics. The principal components (PC) are extracted using Pearson correlation coefficient and Varimax rotation (Kaiser, 1958).

5. Results and interpretation

5.1. Modern dust concentrations

The monthly data on atmospheric dust concentration for Sidi Ali (Fig. 4a) show a clear peak during late summer (July, August), whereas there is low dust input during winter (December, January). The highest interannual fluctuations occur during spring (especially during April and May) as indicated by high standard deviations. Fig. 4b shows the relative quarterly dust input brought from every wind direction (black, large) and the relative accumulated number of days with wind blowing from every wind direction (white, small). Currently, dust is brought from all directions towards Lake Sidi Ali, however, mostly from southern and south-western directions (61%). Only minor proportions derive from northern, north-eastern and north-western origins (5%).

5.2. Build-up of sediment provenance parameters

Siliciclastic element ratios are based on terrestrial XRF samples. Sampling sites, geographical coordinates and element data are documented in Fig. 2 and the Supplementary Online Material. The volcanic ashes and lapilli that solely occur to the north of Lake Sidi Ali present extraordinarily high Ni/Al, Cr/Al, Ti/Al and low K/Ti ratios (Fig. 5). Therefore, we are able to distinguish the volcanic samples robustly from all non-volcanic terrestrial samples and should be able to provide a geochemical northern provenance source by these ratios.

However, at the local scale, Cr/Al versus Ni/Al ratios do not show a consistent geo-chemical separation of the sampling sites within the lake's catchment (Fig. 5a) because volcanic and non-volcanic samples reveal a broad statistical deviation. In contrast, the local K/Ti versus Ti/Al plots of volcanic and non-volcanic terrestrial samples are in line with the samples from the lake core itself (Fig. 5b), however, a higher sample density is required to provide a significant spatial separation of the catchment XRF samples in distinct local provenances. This is especially required for non-volcanic terrestrial samples.

This situation differs within the regional and supra-regional K/Ti versus Ti/Al and Cr/Al versus Ni/Al scatter plots (Fig. 5c to f) that indicate consistent geochemical separations in northern and southern siliciclastic provenances. At the regional scale, Cr/Al versus Ni/Al and K/Ti versus Ti/Al plots show a clear geochemical separation of the terrestrial XRF samples from south to north (Fig. 5c and d). The Cr/Al versus Ni/Al and K/Ti versus Ti/Al scatter plots from Sidi Ali core itself are characterised by an intermediate position between southern and northern terrestrial XRF samples and by similar inclinations. Therefore, we postulate that Sidi Ali core samples with low Cr/Al, Ni/Al and Ti/Al ratios and with an enhanced K/Ti ratio reflect a more southern provenance of the siliciclastic material and vice versa.

At the supra-regional scale, terrestrial XRF samples from the

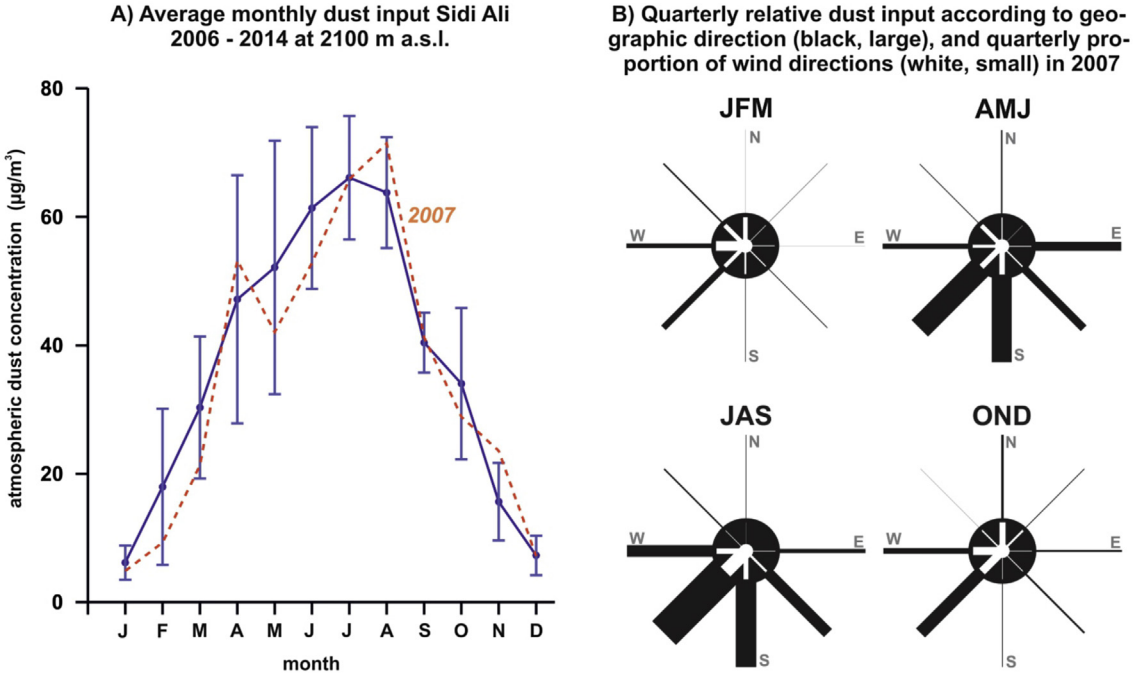

Fig. 4. Dust concentrations at Lake Sidi Ali (N 33.071111, E -4.995833). A) Dust concentrations of the BSC-DREAM8b model v2.0 between 1st January 2006 and 31st December 2014. B) Quarterly relative dust input in 2007 according to geographic direction (black, large), and quarterly proportion of wind directions (white, small).

pre-Saharan Basin and the Anti-Atlas foothills (Fig. 5e and f) show low Cr/Al, Ni/Al and Ti/Al and enhanced K/Ti ratios as well, allowing a spatial prolongation of the probable Sidi Ali detrital sources further south and south-west. Furthermore, secondary data from the Western and Central Sahara (Fig. 5e) show low Cr/Al and Ni/Al ratios, supporting evidence for a probable remote Saharan source area of siliciclastic deposits in Lake Sidi Ali. This corresponds also with low Ti/Al and enhanced K/Ti ratios of Saharan dust from the Canary Islands (Fig. 5f).

Two additional element ratios, Ti/Th and Ti/Zr, reveal an interesting pattern that might be useful for a geographical separation of varying silici-clastic provenances. Muhs et al. (1990) used Ti/Th and Ti/Zr ratios for the detection of remote Saharan dust at Caribbean and Western Atlantic islands. Intriguingly, the Ti/Th and Ti/Zr ratios do not reflect remote provenances of the silici-clastic fraction but might be good proxies for proximal siliciclastic origin at Sidi Ali.

The local terrestrial samples from the Sidi Ali volcano in the north of the lake's catchment differ geochemically from the Jurassic carbonate rocks in the south of the catchment (Fig. S2, Supplementary Online Material). The geographical separation is visible in the combined Ti/Th and Ti/Zr provenance plots (Fig. 6a). Here, the grey dots from the lake's core show an intermediate position between the more southern oriented surface samples from the Jurassic carbonate rocks and the northern oriented surface samples from the Sidi Ali volcano. However, the surface sampling density is quite low and thus we interpret the data set only very carefully.

At the regional scale, Ti/Th and Ti/Zr ratios from the High Atlas and the Upper Moulouya Basin show lower ratios than the Middle Atlas volcanic and non-volcanic samples (Fig. 6b). This might indicate a general trend for regional separation between southern and northern provenances. However, the plot of the Sidi Ali core samples (grey dots, Fig. 6b) does not reveal an intermediate position within the scattered plot of the regional-scale terrestrial samples but lies significantly outside their probable distribution. This indicates that the regional-scale Ti/Th and Ti/Zr ratios do not build up the Ti/Th and Ti/Zr ratios within the core. Hence, there is no evidence for a geomorphological coupling between the regional-scale Ti/Th and Ti/Zr sampling zones and the Ti/Th and Ti/Zr ratios within the core.

At the supra-regional scale, Ti/Th and Ti/Zr ratios from the Anti-Atlas and the pre-Saharan depression (Fig. 6c) similarly do not show any geochemical correspondence with the Ti/Th and Ti/Zr ratios from Sidi Ali core. Furthermore, the samples from the pre-Saharan depression and the Anti-Atlas are strongly scattered and show no clear geographical clusters.

Finally, low Cr/Al, Ni/Al, Ti/Al and enhanced K/Ti ratios display significant southern provenance signals at regional (High Atlas, Upper Moulouya, Middle Atlas) and supra-regional (Anti-Atlas foothills and the pre-Saharan Basin) scale (Fig. 7). In contrast, Ti/Th and Ti/Zr ratios indicate local provenance signals that might be probably also the case for varying Ti/Al and K/Ti ratios (Fig. 7).

5.3. Grain-size end-member analysis

The grain size end-member modelling reveals three robust end-members rEM1 to rEM3 within 76 similarly likely model runs. A fine silty rEM1 with a main mode between 5 and 8 µm (maximum at 6.6 µm, black line in Fig. 8) represents 45.0% of the variance and dominates the lower parts of the core (1600-2000 cm depth, ca. 70–90% of all detrital material, Fig. 9a). In contrast, rEM1 reveals minimum scores around 20% in the top 400 cm of the core.

The medium silty rEM2 (red lines in Fig. 8) has a rather broad mode between 10 and 25 µm and a maximum at 13 µm with high uncertainty range, i.e. high diversity of this rEM, and it represents only 12.7% of the variance in all the samples. Also the downcore scores show rather marked fluctuations of this rEM (Fig. 9a).

The coarse-silty to fine-sandy rEM3 (maximum at 46 µm, 42.3% of the mean total variance, green line in Fig. 8) has a very low uncertainty in its loadings, reflecting a high robustness similar to rEM1. Its downcore scores show high average contributions of this rEM (>50%) during the intervals 700-1500 cm and above 400 cm. In the topmost sediments, this rEM contributes as much as 80–100% (Fig. 9a).

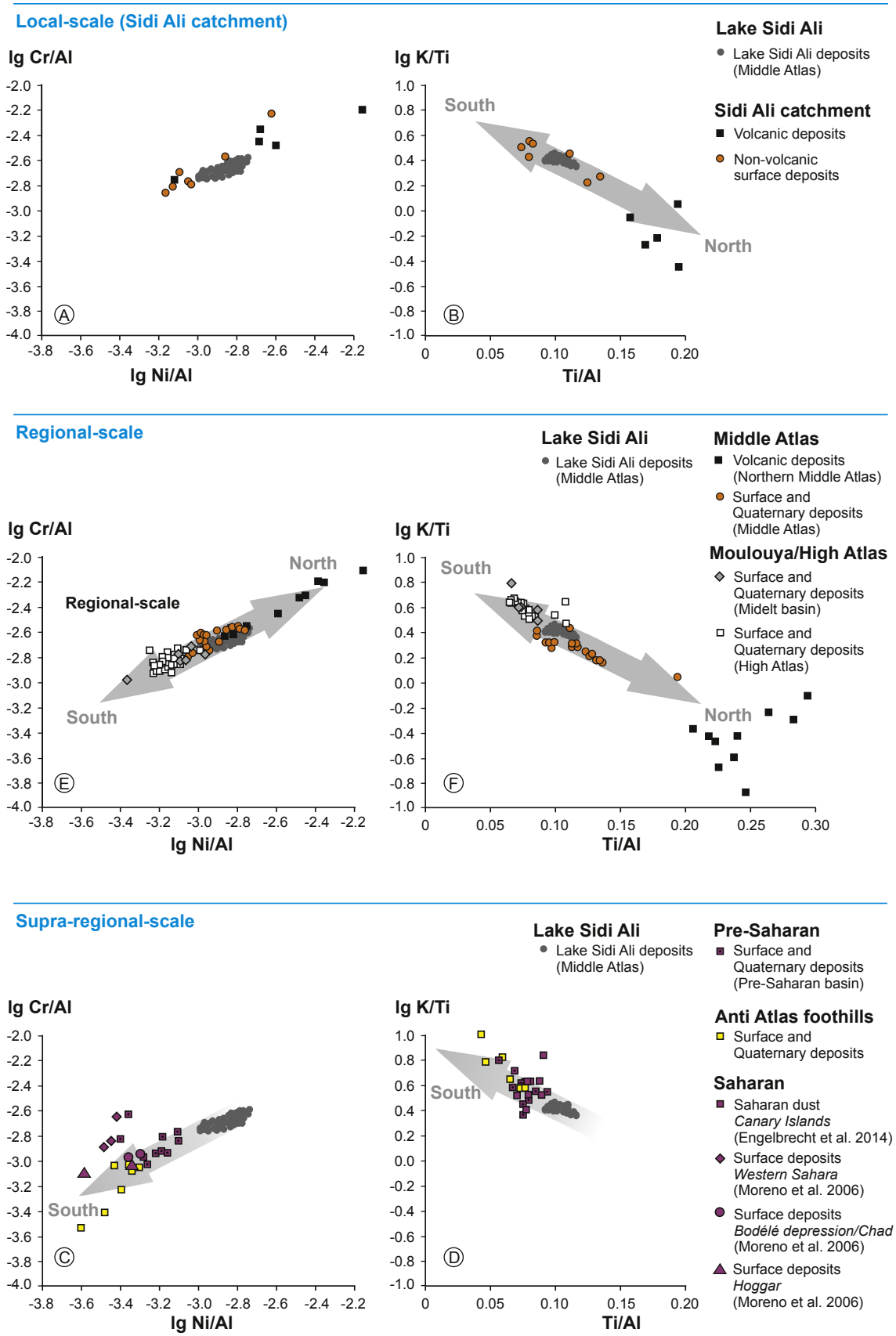

Fig. 5. Combined Cr/Al versus Ni/Al and K/Ti versus Ti/Al provenance plots from terrestrial XRF samples (this study) and from the Sidi Ali core (this study): A and B) local-scale (Sidi Ali catchment); C and D) regional-scale; E and F) supra-regional scale. The supra-regional provenance plots also consider secondary data from the Canary Islands (Engelbrecht et al., 2014), Western Sahara, Hoggar Mountains and Bodélé Depression (Moreno et al., 2006).

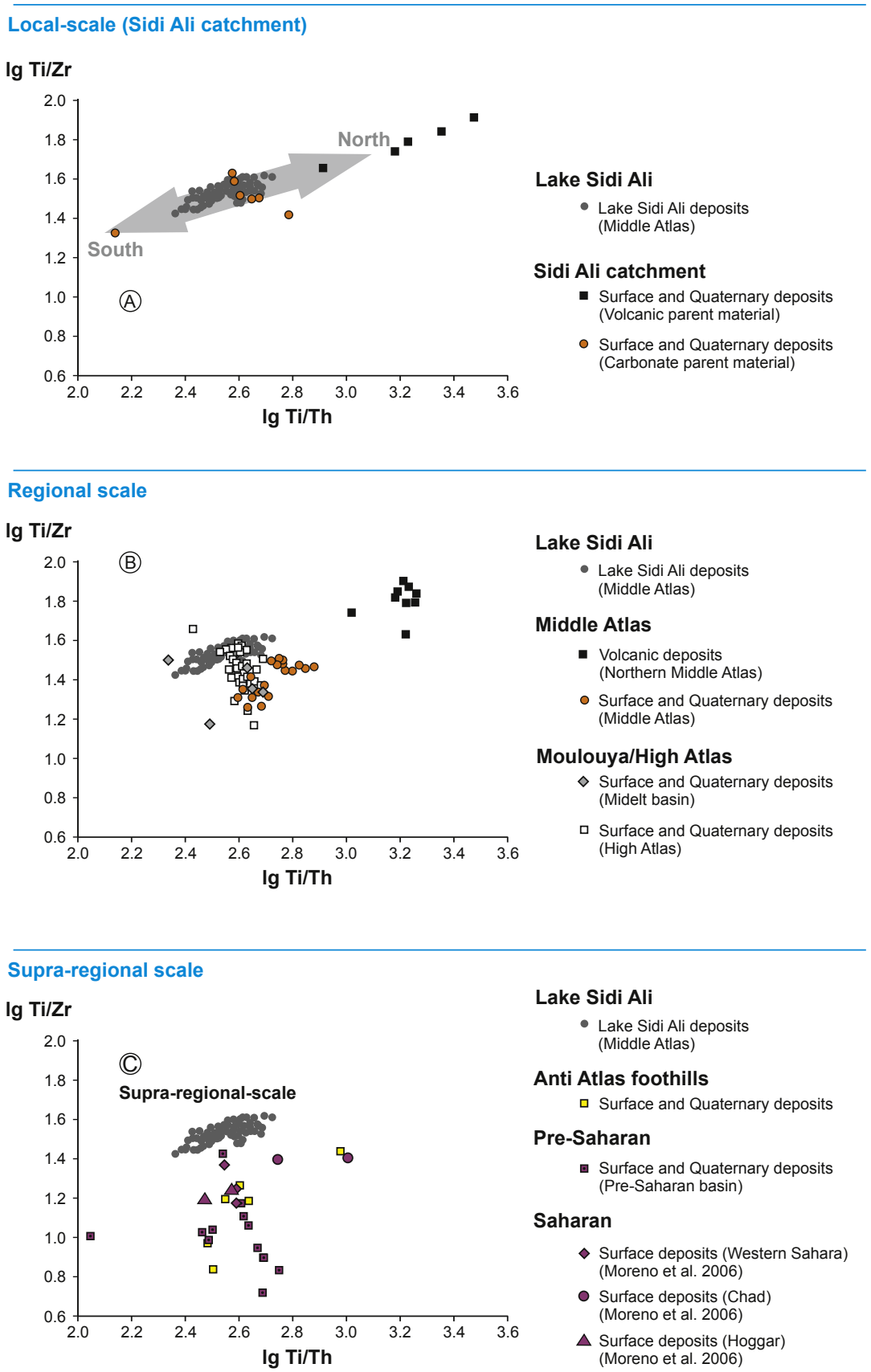

Fig. 6. Combined Ti/Th versus Ti/Zr provenance plots from terrestrial XRF samples (this study) and from the Sidi Ali core (this study): A) local-scale (Sidi Ali catchment); B) regional-scale; C) supra-regional scale. The supra-regional provenance plots also consider secondary data from the Western Sahara, Hoggar Mountains and Bodélé Depression (Moreno et al., 2006).

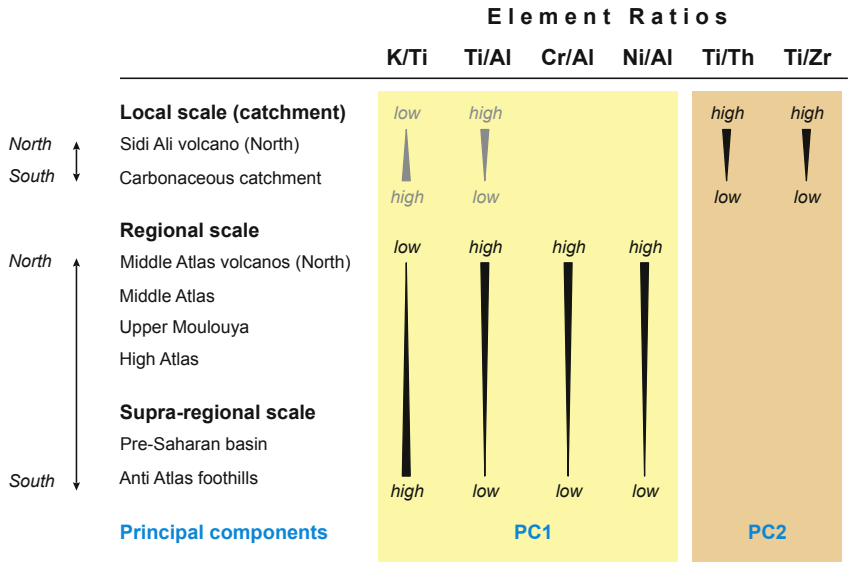

Fig. 7. Combined illustration of element provenance signals. The headline shows the selected element ratios in this study. The left column shows the geographical transects from local to supra-regional-scale. Arrows with increasing or decreasing widths indicate consistent provenance signals for the individual element ratios. Black arrows show clear characteristics, grey arrows present more tentative characteristics. The footer shows the dominant loading of individual element ratios within the Sidi Ali PC1 and PC2 principal components.

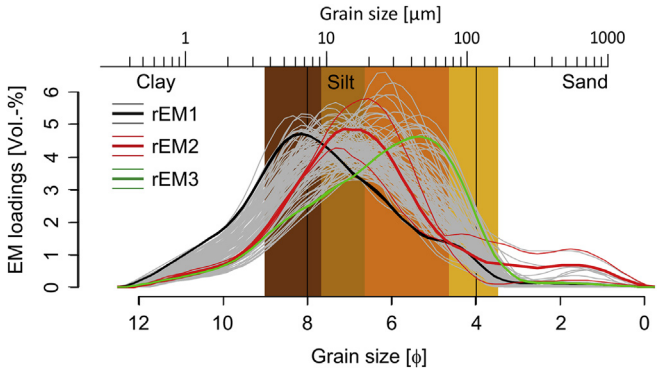

Fig. 8. Three robust Sidi Ali grain size end-members (rEM). Fine silty rEM1 (black) is interpreted as remote dust, medium silty rEM2 (red) as regional dust, and the coarse silty to fine sandy rEM3 represents a more local component (green). Mean and standard deviation of the subpopulations are shown as bold and thin lines. Brown, orange and yellow bars mark characteristic grain size end-members of Dietze et al. (2014), i.e. remote, coarse regional and coarse local dust, respectively. (For interpretation of the references to colour in this figure legend, the reader is referred to the web version of this article.)

5.4. Extraction of three principal components

In a first ordination we include seven siliciclastic provenance proxies (K/Ti (Spectro), K/Ti (ITRAX), Ti/Al, Cr/Al, Ni/Al, Ti/Th and Ti/Zr) and three grain-size end-members (rEM1 to rEM3) into a principal component analysis (PCA). The results of the first PCA indicate slight correlations between grain size end-members and some siliciclastic provenance proxies for the total core record. However, these correlations are not visible in step-by-step correlations of fractional core sections. In a second run, we replace the grain size end-members with two end-member ratios (rEM3/rEM1 and rEM2/rEM1). The resulting principal components indicate no significant correlation between grain size and provenance proxies for the total record but now emphasize synchronous pattern between grain sizes and provenances at higher frequencies. Therefore, we present the results of the second PCA here that includes three principal components (PCs) from provenance and grain size proxies with eigenvalues >1. The 1st to 3rd PCs represent a cumulative variance of 88.6% (Table 1). The 1st principal component (PC1) reveals high loadings for Cr/Al, Ni/Al, and Ti/Al ratios and highly negative loadings for K/Ti (Spectro) and K/Ti (ITRAX) ratios (Fig. 10). Low scores of PC1 reflect an increased southern provenance signal of the siliciclastic fraction at regional and supra-regional scales. The 2nd principal component (PC2) represents changing origins of siliciclastic materials at the lake's catchment-scale due to high loadings in Ti/Th and Ti/Zr. Hence, maxima (minima) of PC2 represent an enhanced local provenance signal from the volcanoes (calcareous areas) within the catchment. The 3rd principal component (PC3) reveals high loadings in grain-size end-member ratios EM3/EM1 and EM2/EM1. Low PC3 scores indicate a dominance of fine detrital grains.

6. Discussion

6.1. Reconstruction of aeolian dynamics using the grain-size end-members

Despite the lack in correlation between provenance proxies and grain-size ratios for the total core record (Table 1), size-dependent sorting of siliciclastic grains with transport distance and energies might allow a general source designation of certain grain size subpopulations. The fine silty rEM1 (mode: 6.6 µm, Fig. 8) and medium silty rEM2 (mode: 13.2 µm) generally correspond with grain size modes of current Saharan dust between 5 and 40 µm (Coudé-Gaussen, 1991; Goudie and Middleton, 2001). The finest rEM1 can be interpreted as atmospheric background dust that is mobilised throughout the year and that can be transported in several km high atmospheric levels over thousands of km (Dietze et al., 2014; Jaramillo-Vélez et al., 2016; Sun et al., 2004; Vandenberghe, 2013). Furthermore, rEM1 represents the fraction of small dust (2-8 µm) consisting of clay mineral aggregates and mono-mineral particle fragments that are currently transported from the Western Sahara and the Sahel towards Europe (Goudie and Middleton, 2006; Stuut et al., 2009). In consideration of a

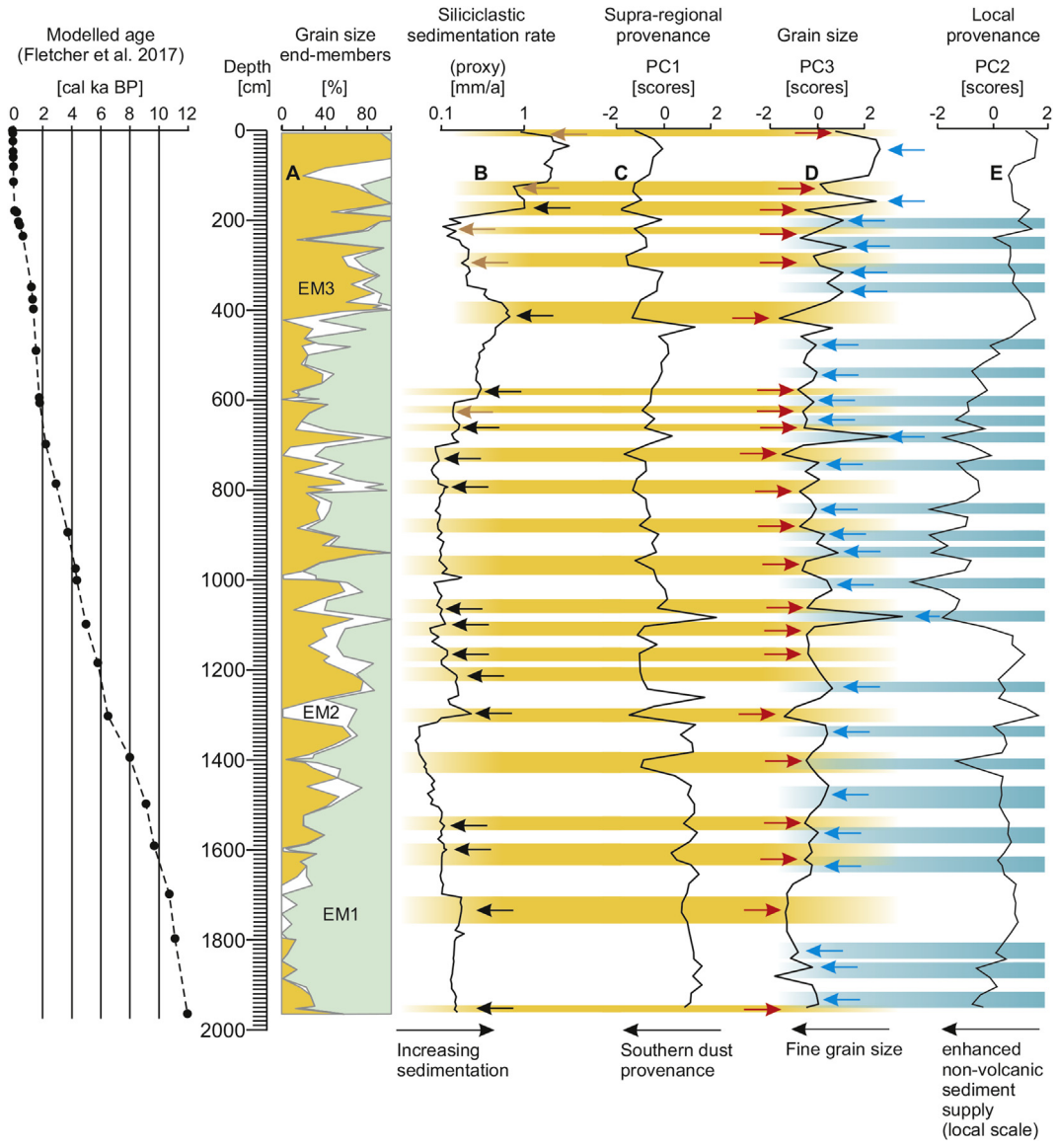

Fig. 9. Sidi Ali grain size end-members (A), Sidi Ali proxy for the siliciclastic sedimentation rate (B) and Sidi Ali downcore scores of principal components, showing: C) Changes in regional to supra-regional-scale provenances (PC1 provenance proxy); D) Changes from coarse (local to regional) to fine (remote) dust (PC3 grain size proxy); and E) Changes in local-scale provenances (PC2 provenance proxy). Yellow bars indicate peaks in southern dust provenance, red arrows show peaks in grain size fining, black arrows show peaks in sedimentation, brown arrows indicate troughs in sedimentation, blue bars indicate enhanced non-volcanic sediment supply at local scale, and blue arrows show grain-size coarsening. Black circles show the Bayesian modelled ages (Fletcher et al., 2017). The 95% probability curve of the age model is shown in Fig. 3. (For interpretation of the references to colour in this figure legend, the reader is referred to the web version of this article.)

Table 1
Three rotated principal components with cumulative variances, eigenvalues and loadings. Highly positive and negative loadings are marked in bold.

	PC1: 1st component	PC2: 2nd component	PC3: 3rd component
Eigenvalue	3.69	2.27	2.01
Cumulative variance [%]	41.03	66.30	88.60
Ti/Al	**0.873**	0.397	−0.008
K/Ti (Spectro)	**−0.764**	−0.214	0.125
K/Ti (ITRAX)	**−0.863**	−0.207	0.337
Ti/Zr	0.054	**0.920**	0.089
Ti/Th	0.263	**0.914**	0.112
Cr/Al	0.937	−0.120	−0.215
Ni/Al	0.749	−0.537	−0.314
EM3/EM1	−0.241	0.031	**0.931**
EM2/EM1	−0.175	0.208	**0.919**

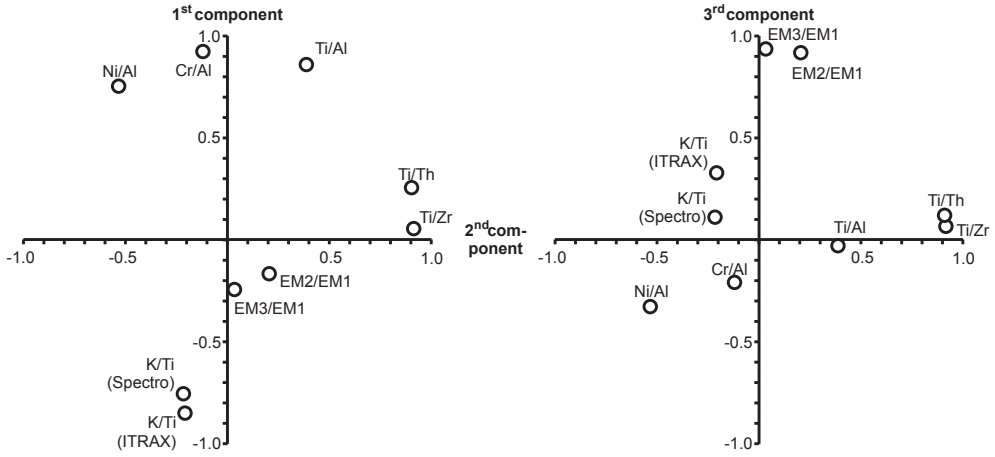

Fig. 10. Biplots of the principal components (PC): A) PC1 (supra-regional provenance proxy) vs. PC2 (local provenance proxy); B) PC3 (grain size proxy) vs. PC2 (local provenance proxy).

totally different geomorphic setting, we exclude a fluvial origin of the fine silty rEM1 although it has similar modes to offshore fluvial end-members (e.g. Holz et al., 2007; Tjallingii et al., 2008). The steep valleys of the lake's catchment, torrential runoff events and short transport distances do not allow the supply of large amounts of fine silt as the result of a fluvial sorting process.

The medium silty rEM2 rather reflects regional dust, but due to its heterogeneity (Fig. 8) we assume a higher diversity in sorting processes, probably as a result of the variable mountain topography. The characteristic grain size suggests a transport of the particles to the lake by short-term low-level suspension clouds (Dietze et al., 2014; Vandenberghe, 2013).

The specific location of Lake Sidi Ali in the mountainous zone of the Middle Atlas might explain why rEM1 and rEM2 dust particles are finer than aeolian components from Saharan margin offshore studies that reveal a characteristic mode between 18 and 35 μm (Holz et al., 2007; Moreno et al., 2002; Tjallingii et al., 2008). Topographic barriers cause uplift of dust-transporting air masses (Stuut et al., 2009). However, we argue that the mountainous altitude of the lake (2.080 m a.s.l.) significantly reduces the size of the accumulating aeolian particles. This effect is well-known from the Canary Islands. Torres-Padrón et al. (2002) recorded multiple Saharan dust events at Gran Canaria in an altitude of 1.980 m a.s.l. that feature maxima varying between 2 and 5 μm. In contrast, Menéndez et al. (2007) document Saharan dust events at the Grand Canary lowlands that reveal coarser grain sizes with maxima ranging between 16 and 62 μm.

Generally, modern Saharan dust within the atmospheric boundary layer of the North Saharan desert margin reveals size distributions over an extremely wide range from nanometre sizes up to hundreds of micrometres (Kandler et al., 2009). However, above the boundary layer a relative enrichment of a fine silty to medium-silty dust fraction is detectable (Kandler et al., 2009). *In situ* aircraft measurements of Saharan dust originating from Mali, Mauritania and Algeria (Ryder et al., 2013a) and of the Saharan Air Layer over the Canary Islands (Ryder et al., 2013b) reveal noticeable grain size means between 5 and 20 μm 1 km above of the ground.

The coarse-silty to fine-sandy rEM3 can be interpreted as coarse local dust (Stuut et al., 2009) originating probably from the lake's catchment and adjacent intra-montane basins (Dietze et al., 2014). Alternatively, rEM3 might derive from local alluvial sources that feature a dense net of ephemeral streams and torrents. As this end member dominates in the topmost section of the core, we assume a relationship to human induced soil erosion.

6.2. Dust supply to Lake Sidi Ali

The comparison of PC1 and PC2 provenance proxies with the PC3 grain-size proxy might allow the identification of prominent dust sources and associated atmospheric circulation patterns. PC1 represents changing regional to supra-regional XRF provenance signals at Sidi Ali as it comprises high loadings in Cr/Al, Ni/Al, Ti/Al and low loadings in K/Ti. Despite a lack of significant correlation between PC1 and PC3 for the entire core record, minima in PC1 downcore scores (Fig. 9c, yellowish bars) are chronostratigraphically in phase with minima of the PC3 grain size proxy (Fig. 9d, red arrows), indicating enhanced southern provenances during phases of grain size fining. This is also indicated by the running correlation between PC1 and PC3 (Fig. 11b). The values are clearly positive for almost the entire Holocene sequence.

Furthermore, we provide in the Supporting Online Material grain size-specific XRF analyses that test our hypothesis of a coupling of enhanced southern provenances and grain size fining in the core. The grain size-specific-XRF analyses does not show a response for K/Ti and Ti/Al. Probably, the pre-treatment with 10% HCl lead to a leaching of specific elements or K/Ti and Ti/Al ratios are affected also by local geomorphological processes at catchment-scale as already indicated in Figs. 5 and 7. However, noticeably lower Cr/Al and Ni/Al ratios for particles <20 μm confirm that these southern provenance signals correspond with grain size fining (Supplementary Online Material). We suggest that Holocene phases of enhanced southern provenance signals and grain size fining represent relative maxima in remote Saharan dust supply at Sidi Ali. This is similar to maxima of modern dust origins during spring and summer (Fig. 4b) and similar to large-scale dust trajectories from the Sahel and Central Sahara towards the Northwest African desert margin (yellow arrows in Fig. 1; Ashpole and Washington, 2013; Schepanski et al., 2016; Stuut et al., 2009).

We recognise that our geochemical sampling transect at the North African desert margin (Fig. 2) might not represent the full size of the source area of remote dust deposited at Sidi Ali. However, we follow the dust mixing model of Scheuvens et al. (2013). The authors suggest a characteristic average geochemical composition of dust due to dust homogenisation processes at the regional scale. During dust entrainment several local dust signals may externally mix. We assume that this process might be also active during large-scale dust transport processes with intercalated, multiple dust mobilisation and deposition events (Westphal et al., 1988). In other words, the geochemical XRF ratios of our terrestrial sampling transect might encompass also geochemical

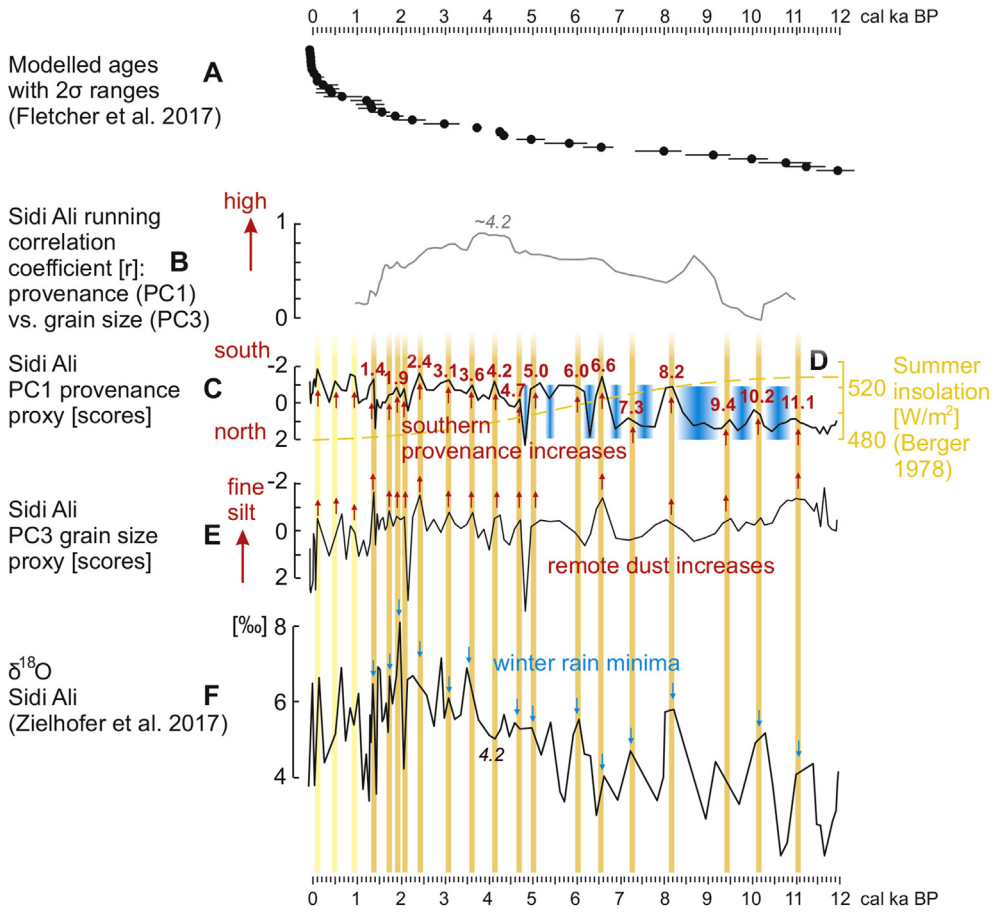

Fig. 11. Coupling between North African dust proxies and Western Mediterranean hydro-climate derived from Lake Sidi Ali core, showing: A) Modelled ages with 2 σ ranges (Fletcher et al., 2017); B) Positive running correlation between the 1st Principal Component (PC1) and the 3rd Principal Component (PC3); C) Sidi Ali 1st principal component (PC1) [inverse scale] representing the siliciclastic provenance signal at regional to supra-regional scale. The red numbers [cal ka BP], red arrows and yellow bars indicate enhanced southern provenance signals, pale yellow bars are similar to yellow bars but might be also the result of pronounced human impact in the Sidi Ali catchment; D) summer insolation curve (65°N, June, Berger, 1978) [W/m^2]; E) Sidi Ali 3rd principal component (PC3) [inverse scale] representing grain size fining. The red arrows indicate peaks in grain size fining; F) Sidi Ali $\delta^{18}O$ stable isotope record from ostracod shell material of closely related species *Fabaeformiscandona* sp. and *Candona* sp. (Zielhofer et al., 2017). $\delta^{18}O$ maxima represent Western Mediterranean winter rain minima. The Blue arrows indicate Western Mediterranean winter rain minima that coincide with increases in Saharan dust supplies. (For interpretation of the references to colour in this figure legend, the reader is referred to the web version of this article.)

fingerprints from dust sources further south.

PC2 comprises high loadings in Ti/Th and Ti/Zr (Table 1, Fig. 10). Hence, PC2 downcore scores reflect the local, catchment-scale XRF provenance signal at Sidi Ali and there are noticeable PC2 minima (Fig. 9e, blue bars) that correspond with maxima of the PC3 grain size proxy (Fig. 9d, blue arrows). We interpret PC2 minima that coincide with PC3 maxima as centennial-scale phases of increased detrital input from the karstic, non-volcanic zone of the lake's local environment. We suppose a more complex local sediment transport and deposition history, maybe via fluvial re-deposition of local to regional dust that was deposited on the hillslopes previously (similar as described by Dietze et al., 2012), but this needs further study, which is not the focus here.

Both remote Sahelian and Saharan and local dust sources currently contribute to the dust fraction deposited over the Atlas Mountains. Whereas dust originating from local sources is directly affected by local weather conditions including local and regional atmospheric circulation patterns such as local wind systems, dust that originates from remote source areas has travelled long distances within the atmosphere to eventually reach the deposition area. The general transport pathway is the result of the atmospheric circulation at a larger (e.g. sub-continental) scale and atmospheric features such as the West African Monsoon, the Harmattan, and heat low formation that steer the transport routes (Schepanski et al., 2016). Dust from Sahelian sources can be transported northward towards the Atlas mountain region, in particular during summer. At this time of the year, the West African Monsoon circulation and the Saharan Heat Low in concert allow Sahelian dusty air masses to propagate northward, frequently remaining stationary for up to several days over central Mauritania and western Algeria (Ashpole and Washington, 2013).

6.3. Millennial-scale peaks in dust supply during the Early and Mid-Holocene

During the Early Holocene and the first half of the mid-Holocene the overall pattern of the Sidi Ali record shows relatively low siliciclastic sedimentation rates (Fig. 9b) and high PC1 values (Fig. 11c, blue bars) generally indicating reduced dust influxes from southern origin. However, multiple shifts towards southern provenance modes (Fig. 11c, red arrows) that coincide with abrupt grain size finings (Fig. 11e, red arrows) and occasional short-term increases of the Sidi Ali siliciclastic sedimentation rate (Fig. 9b, black arrows) reveal millennial-scale fluctuations of southern dust increases. Keeping 2σ ranges of the age model in mind (Fig. 11a) this southern dust increases occurred at about 11.1, 10.2, 9.4, 8.2, 7.3, 6.6, 6.0 and 5.0 cal ka BP (Fig. 11, yellowish bars). This coupling between increased southern provenances (low PC1) and grain-size fining

(low PC3) corresponds with a positive running correlation (Fig. 11b).

Furthermore, parallels between the millennial-scale peaks in southern dust supply and the $\delta^{18}O$ winter rain proxy from the same core (Zielhofer et al., 2017, Fig. 11f) indicate a chronological coupling of Saharan dust increases and North-Atlantic hydro-climate: there is a noticeable coincidence of southern dust increases (Fig. 11c and e) and Western Mediterranean winter rain minima (Fig. 11f) that, again, coincide with North Atlantic cooling events (Bond et al., 2001; Jiang et al., 2015; Zielhofer et al., 2017) during the Early and Mid-Holocene. Prominent Early Holocene North Atlantic cooling episodes result from millennial-scale weakening of the Atlantic Meridional Overturning Circulation (Fletcher et al., 2013) due to freshwater outbursts from the Laurentide ice sheet during the deglaciation (Wanner et al., 2015). We assume that Early Holocene North Atlantic cooling episodes result in a significant northward shift of Atlantic cyclone trajectories with cold and dry conditions over Southwestern Europe and Mediterranean North Africa (Fletcher et al., 2013; Zielhofer et al., 2017) but also with northward intrusions of dust enriched Saharan air masses. This is supported by Swezey's (2001) review of Holocene Saharan aridity phases. The author indicates enhanced aeolian sediment mobilisation at about 10 cal ka BP, between 8.4 and 8 cal ka BP and at about 7.5 cal ka BP at the North Saharan margin but also at several other locations throughout the Sahara.

However, it is important to note that Early Holocene PC1 scores (Fig. 11c) show only slight changes towards more southern dust supplies around 9.4–9.2 and 7.4–7.2 cal ka BP although the Sidi Ali $\delta^{18}O$ curve reveals significant Atlantic winter rain minima at that time (Fig. 11f). This might indicate that the Early Holocene dust supply was influenced also by climatic mechanisms active in a more southern domain and not only by hydro-climatic changes in the North Atlantic realm. In this context, it is noticeable that North Atlantic forcing signals around 9.4–9.2 and 7.4–7.2 cal BP are detectable within the Sidi Ali winter rain record but seem to be absent within the sea surface temperature record at the Western Saharan site 658C off Mauretania (deMenocal et al., 2000b).

Furthermore, a comparison of the Sidi Ali dust provenance record with hydro-climatic records from the West African monsoon domain indicates a bimillennial pulsing of aridity phases at about 10.2, 8.2 and 6.0 cal BP (Fig. 12b) that is probably in evidence at a *trans*-Saharan scale. Keeping age uncertainties in mind, this might be shown by leaf wax-based reconstructions of palaeoprecipitation along the West African shore line (Fig. 12d and f; Tierney et al., 2017) but also by the dust-based humidity index at Site GeoB7920-2 off Mauretania (Fig. 12e; Tjallingii et al., 2008) as well as large-scale declines in population densities in the Central and Eastern Sahara at about 10.2, 8.2, 6.6 and 6.0 cal ka BP (Manning and Timpson, 2014). Overall, major phases of southern dust supply at the North Saharan desert margin significantly coincide with North Atlantic forcing signals within the Sidi Ali record (Fig. 12a), but the bimillennial pulsing resembles humidity shifts that are more typical for the West African monsoon domain (blue and orange bars in Fig. 12). Therefore, we assume that the Early to Mid-Holocene dust record at Sidi Ali reflects sub-Saharan climatic forcing mechanisms, which are active at a *trans*-Saharan scale. However, Saharan aridity phases are chronologically in phase with millennial-scale decreases in Western Mediterranean winter rain (Fig. 12a) that might coincide with cooling events in the North Atlantic realm (Bond et al., 2001; Jiang et al., 2015).

Regarding major source areas for modern Saharan dust (Fig. 1, blue, green, yellow and orange squares, from Schepanski et al., 2009), it is noticeable that these are located predominantly in the Sub-Saharan, monsoonal domain. In this context it is interesting that the PC1 southern provenance proxy at Sidi Ali (Fig. 12b) and the oxygen index in the Eastern Mediterranean Sea (Fig. 12c; Schmiedl et al., 2010) indicate an overall comparable pattern during the Early Holocene and the first half of the Mid-Holocene. The oxygen index in the Eastern Mediterranean Sea is influenced by freshwater fluxes from the north-eastern Mediterranean Basin but also from the Nile River, the latter controlled by humidity shifts in the Nile headwaters within the East African monsoon domain (Blanchet et al., 2013a, 2013b; Rossignol-Strick et al., 1982). Thus, low oxygen indices in the Eastern Mediterranean Sea coincide with humidity in the Eastern Mediterranean and the East African monsoonal rain belt. Especially the low oxygen sapropel layers between 10 and 7 cal ka BP (Fig. 12c), with the short-term interruption at 8.2 cal ka BP, are in phase with the PC1 southern provenance proxy (Fig. 12b) at Sidi Ali. Therefore, synchronous *trans*-Saharan aridity phases might be detectable alongside the entire sub-Saharan rain belt during the Early Holocene and the first half of the Mid-Holocene.

6.4. Multiple abrupt dust increases at the end of the African Humid Period

At orbital scale, there is an overall mid-Holocene change towards a southern origin of detrital sediment supply at Sidi Ali. Whereas the summer insolation curve (Berger, 1978) shows a gradual decrease from the Early to the Late Holocene (Fig. 11d), the Sidi Ali PC1 provenance proxy reveals a mid-Holocene shift from positive to negative scores (Fig. 11c) indicating an enduring southern origin of detrital sediment supply from 4.7 cal ka BP until present. We assume a Saharan drying trend here due to the continuous southward migration of the northernmost position of the ITCZ in North Africa during the Holocene (deMenocal et al., 2000a; Tierney and deMenocal, 2013; Tierney et al., 2017). However, the continuous desiccation is characterized by multiple major southern dust increases at 10.2, 8.2, 6.6, 6.0 and 5.0 cal ka BP and minor peaks at 9.4 and 7.3 cal ka BP indicating abrupt Saharan drying events before the 'southern dust mode' was finally established at 4.7 cal ka BP (Fig. 11c and e). It is noticeable, that major southern dust increases are characterised by strong PC1 shifts from highly positive scores to highly negative ones (Fig. 11c). This pattern might indicate abrupt shifts in Saharan aeolian dynamics and might support the general concept of abrupt ecosystem shifts in the Western Sahara at the end of the African Humid Period (deMenocal et al., 2000a; Egerer et al., 2016). However, multiple Saharan provenance peaks at Sidi Ali seem to reveal a synthetic pattern of a gradual Saharan desiccation as documented in Eastern (Kuper and Kröpelin, 2006) and Central (Kröpelin et al., 2008) Saharan studies and the abrupt shift towards a dry ecosystem (deMenocal et al., 2000a) in the Western Sahara at ~5 cal ka BP. In contrast to the Western Saharan end of the African Humid Period at ~5 cal ka BP, the Sidi Ali dust record supports the evidence of an earlier onset of Saharan aridity (6.6–6.0 cal ka BP) as already indicated by Gasse et al. (1990), Kuper and Kröpelin (2006), Shanahan et al. (2015) and Tierney et al. (2017). This is also in agreement with Saharan dust records from South-western (Jiménez-Espejo et al., 2014), Central (Le Roux et al., 2012) and Eastern Europe (Longman et al., 2017) that indicate a significant increase in Saharan dust already at approx. 7 to 6 ka.

6.5. North Atlantic coupled multi-centennial-scale aeolian history (Late Holocene)

Mid- to Late Holocene increases in Saharan dust at 4.7, 3.6, 3.1, 2.4, 1.9, and 1.4 cal ka BP (Fig. 11c and e) coincide with Western Mediterranean winter rain minima (Fig. 11f) that correspond predominantly with North Atlantic warming (Jiang et al., 2015) and accordingly positive NAO-like conditions (Zielhofer et al., 2017) in

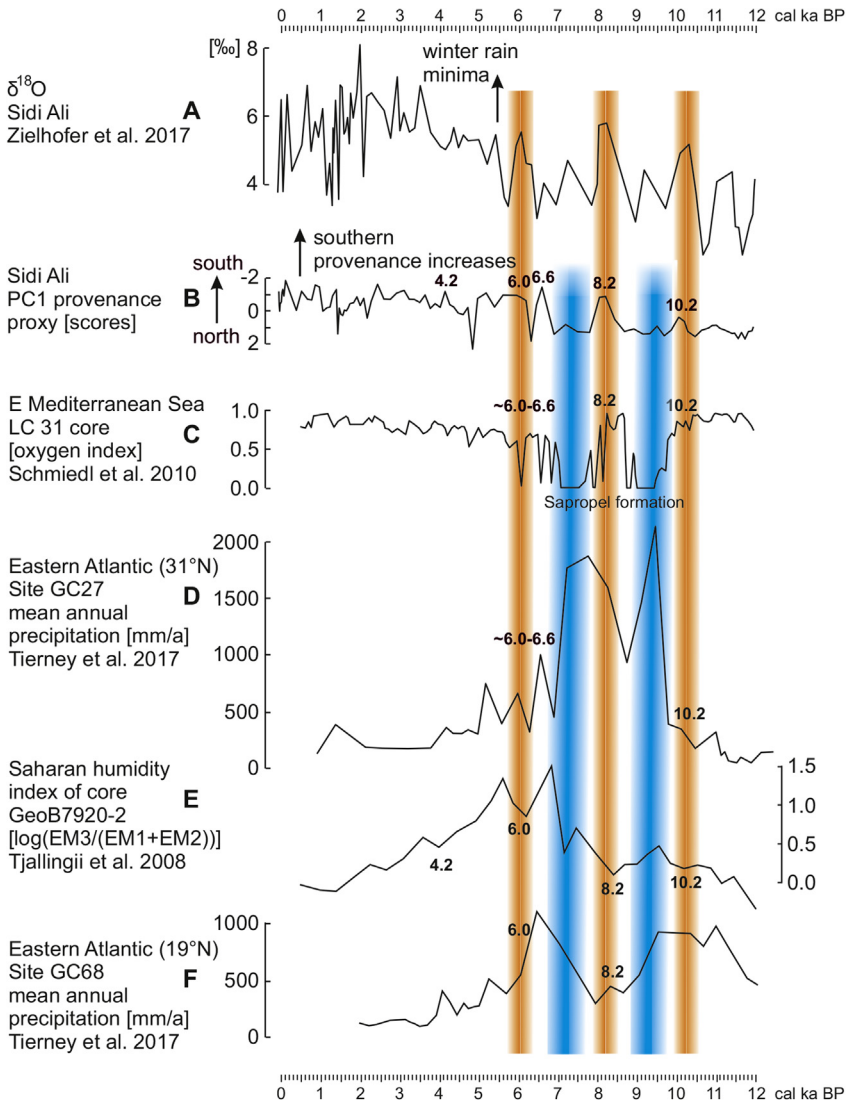

Fig. 12. Correspondence of Western Mediterranean winter rain minima and *trans*-Saharan aridity phases, showing: A) Sidi Ali $\delta^{18}O$ stable isotope record (Zielhofer et al., 2017). High values indicate Western Mediterranean winter rain minima; B) Sidi Ali 1st principal component (PC1) [inverse scale] representing the detrital provenance signal at regional to supra-regional scale (this study). The black numbers [cal ka BP] indicate major phases of enhanced southern provenance; C) Oxygen index of LC 31 core in the Eastern Mediterranean Sea (Schmiedl et al., 2010). Low indices represent phases of enhanced sapropel formation due to increased freshwater influx into the Mediterranean Sea. Black numbers indicate bimillennial phases of reduced freshwater influx during the Early and Mid-Holocene; D) Mean annual precipitation proxy record [mm/a] derived from leaf wax isotopes at GC27 site (31°N) in the Eastern Atlantic (Tierney et al., 2017). The black numbers [cal ka BP] indicate aridity phases that might correspond with aridity in a *trans*-Saharan scale; E) Saharan humidity index of core GeoB7920-2 [log (EM3/(EM1+EM2))] (Tjallingii et al., 2008). The black numbers [cal ka BP] indicate phases of enhanced Western Saharan dust dynamics; F) Mean annual precipitation proxy record [mm/a] derived from leaf wax isotopes at GC68 site (19°N) in the Eastern Atlantic (Tierney et al., 2017). The black numbers [cal ka BP] indicate aridity phases that might correspond with aridity in a *trans*-Saharan scale. The orange-shaded bars represent probable phases of *trans*-Saharan aridity. The blue-shaded bars indicate synchronicities of Eastern Mediterranean sapropel formation, *trans*-Saharan humidity and reduced Saharan dust supply at Sidi Ali. (For interpretation of the references to colour in this figure legend, the reader is referred to the web version of this article.)

the Western Mediterranean. This is in accordance with meteorological studies (Chiapello and Moulin, 2002; Ginoux et al., 2004; Mahowald et al., 2003; Moulin et al., 1997) that show significant increases in recent Saharan dust fluxes into the Mediterranean Sea and the western subtropical Atlantic during positive stages of the North Atlantic Oscillation.

A noticeable PC1 southern provenance peak (Fig. 11c) and PC3 grain size fining (Fig. 11e) indicate an increase in remote southern dust at 4.2 cal ka BP. This dusty phase reveals the highest positive correlation between PC1 and PC3 in the entire Holocene (Fig. 11b) and corresponds with the 4.2 ka aridity event that was recorded in the broader East African rain belt (Gasse, 2002; Gillespie et al., 1983; Thompson et al., 2002), the Eastern Mediterranean (Cheng et al., 2015; Weiss, 2016) and the Southwest Asian monsoon domain (Staubwasser et al., 2003). Although aridity is also indicated at about 4.2 cal ka BP in the adjacent Central Mediterranean region (Margaritelli et al., 2016), this period coincides at Sidi Ali with an increase in winter precipitation (Fig. 11f, Zielhofer et al., 2017). Cruz et al. (2015) and Wassenburg et al. (2016) document also relatively humid conditions in the Western Mediterranean at that time. The hydrological mismatch within the Sidi Ali core stratigraphy between wet conditions in the Middle Atlas and an enhanced southern dust mobilisation at 4.2 cal ka BP supports the concept of remote dust supply due to Saharan and sub-Saharan aridity.

During the last two millennia the Middle Atlas was affected by a significant increase in human impact (Cheddadi et al., 2015). Accordingly, increased southern dust signals at that time might

reflect a different pattern than before. We assume for the last 1400 years (Zielhofer et al., 2017) a complex interplay between hydro-climatic forces and human impact in the Middle Atlas associated with an overall increase in soil erosion that is in phase with enhanced Sidi Ali sedimentation rates (Fig. 9b). It seems that multiple increases in the southern dust signal (Fig. 11c, pale yellow bars) correspond with reduced siliciclastic deposition into the lake during the last two millennia (Fig. 9b, brown arrows). This might be a result of a relative but not absolute increase in southern dust supply due to short-term reduced soil erosion in the Sidi Ali catchment.

7. Conclusions

A 19.63 m long Lake Sidi Ali core from the Moroccan Middle Atlas (2080 m a.s.l.) within the intercalation zone of North Atlantic and Saharan air masses provides a robustly dated multi-proxy reconstruction of Saharan dust supply for the last 12,000 years.

Under current climatic conditions, the aeolian influx into the study area is dominated by dust of south-western to southern origin during the arid summer season. Inspired by the current origin of major dust influx into the study area, we conducted a northeast-southwest transect of surface sediment sampling sites from the Middle Atlas into the pre-Saharan basin for developing a gradient of probable dust provenances. As a result, we were able to identify four XRF element ratios that indicate changes in regional to supra-regional siliciclastic provenances. Surface sediments in the southern part of the transect reveal significantly lower Cr/Al, Ni/Al, Ti/Al and higher K/Ti ratios than surface samples from Middle Atlas volcanic ashes and lapilli in the North of the transect.

The siliciclastic sediments of Lake Sidi Ali consist of three robust grain size end-members (rEM) of local aeolian or fluvial origin and of regional and remote aeolian origin that have their main modes at 45.7, 13.2 and 6.6 μm. The finest rEM represents the dominant aeolian source within the Middle Atlas mountainous landscape and probably reflects in general a Saharan- and Sahelian-wide Holocene dust proxy.

The results of a principal component analysis indicate that major southern provenance peaks in the siliciclastic fraction are chronostratigraphically exactly in phase with major episodes of grain-size fining at Lake Sidi Ali. This relationship reveals numerous phases of enhanced southern dust supply into the lake.

At orbital-scale there is an overall increase in southern dust provenance from the Early Holocene to the Late Holocene. However, the Northern Saharan dust record indicates that the Saharan desiccation does not reveal a simple gradual pattern but is characterized by multiple southern dust increases at 10.2, 9.4, 8.2, 7.3, 6.6, 6.0 and 5.0 cal ka BP before the 'southern dust mode' was finally established. The Sidi Ali Saharan dust record seems to reveal a synthetic pattern of a gradual Saharan desiccation as recorded from the Eastern (Kuper and Kröpelin, 2006) and Central (Kröpelin et al., 2008) Sahara and the abrupt end of the African Humid Period at ~5 ka in the Western Sahara (deMenocal et al., 2000a; Tierney et al., 2017). Astonishingly, the Sidi Ali record also indicates strong millennial-scale variability in Saharan dust across the end of the African Humid Period.

The compilation of our Northern Saharan dust record with the $\delta^{18}O$ winter rain proxy from the same core indicates that dust increases at the northern Saharan margin are strictly in phase with North Atlantic hydro-climatic variability during the Early Holocene and the first half of the Mid-Holocene. Increases in Saharan dust coincide with Western Mediterranean winter rain minima that again correspond with millennial-scale North Atlantic cooling events at 11.1, 10.2, 9.4, 8.2, 7.2, 6.6, and 6.0 cal ka BP. However, pronounced southern dust provenance recorded at Sidi Ali at 10.2, 8.2 and 6.6–6.0 cal ka BP coincide with a bimillennial pulsing of aridity intervals in the Western Saharan and sub-Saharan domain indicating a probable monsoonal impact on the aeolian history at the North African desert margin with *trans*-Saharan evidence of major aridity phases. Overall, the findings point to significant impacts of Atlantic climate forcing on dust dynamics at the Northern Saharan margins, and also to important interactions between mid- and low-latitude climate forcing in Mediterranean Northwest Africa.

After ~5 cal ka BP, Mid- to Late Holocene increases in Saharan dust at 4.7, 3.6, 3.1, 2.4, 1.9, and 1.4 cal cal ka BP coincide with Western Mediterranean winter rain minima associated with positive NAO-like conditions in the Western Mediterranean. This is consistent with meteorological studies that show significant increases in recent Saharan dust fluxes into the Mediterranean Sea and the western subtropical Atlantic during positive stages of the North Atlantic Oscillation. However, there is a Saharan dust increase at 4.2 cal ka BP that does not correspond with Western Mediterranean aridity but with a humid phase at the Moroccan desert margin. This unusual event supports our theory of a large-scale *trans*-Saharan impact on the Holocene dust history recorded at the North African desert margin.

Acknowledgements

Christoph Zielhofer, Steffen Mischke and William Fletcher as principal investigators thank the German Research Foundation (DFG, ZI 721/9-1), the Federal Ministry of Education and Research (BMBF, 01DH17020) and the Natural Environment Research Council (New Investigator Award to W Fletcher, NE/K000608/1, and NERC RCF dating awards, 1765.1013 and 1809.0414) for generous funding of the fieldwork and lab analyses. The authors are grateful to the Institut National des Sciences de l'Archéologie et du Patrimoine (INSAP, Rabat), the Centre National d'Hydrobiologie et de Pisciculture (CNHP, Azrou) and to the Caidad d'Azrou for helpful support in field and in preparing the expedition. Rik Tjallingii is highly acknowledged for conducting the ITRAX XRF core scanner measurements at GFZ Potsdam. Finally, the authors are grateful to two anonymous reviewers and Ana Moreno for helpful comments and suggestions.

Appendix A. Supplementary data

Supplementary data related to this chapter can be found at http://dx.doi.org/10.1016/j.quascirev.2017.07.010.

References

Albani, S., Mahowald, N.M., Winckler, G., Anderson, R.F., Bradtmiller, L.I., Delmonte, B., François, R., Goman, M., Heavens, N.G., Hesse, P.P., Hovan, S.A., Kang, S.G., Kohfeld, K.E., Lu, H., Maggi, V., Mason, J.A., Mayewski, P.A., McGee, D., Miao, X., Otto-Bliesner, B.L., Perry, A.T., Pourmand, A., Roberts, H.M., Rosenbloom, N., Stevens, T., Sun, J., 2015. Twelve thousand years of dust: the Holocene global dust cycle constrained by natural archives. Clim. Past 11, 869–903.

Aitchison, J., 1982. The statistical analysis of compositional data. J. R. Stat. Soc. Ser. B, Stat. Methodol. 44, 139–177.

Aitchison, J., 1999. Logratios and natural laws in compositional data analysis. Math. Geol. 31, 563–580.

Ashpole, I., Washington, R., 2013. Intraseasonal variability and atmospheric controls on daily dust occurrence frequency over the central and Western Sahara during the boreal summer. J. Geophys. Res. 118, 12915–12926. http://dx.doi.org/10.1002/2013JD020267.

Avila, A., Alarcón, M., Queralt, I., 1998. The chemical composition of dust transported in red rains: its contribution to the biogeochemical cycle of a holm oak forest in Catalonia (Spain). Atmos. Environ. 32, 179–191.

Basart, S., Pérez, C., Nickovic, S., Cuevas, E., Baldasano, J.M., 2012. Development and evaluation of the BSC-DREAM8b dust regional model over Northern Africa, the Mediterranean and the Middle East. Tellus B 64, 1–23.

Berger, A., 1978. Long-term variations of caloric insolation resulting from the earth's

orbital elements. Quat. Res. 9, 139–167.
Blanchet, C.L., Tjallingii, R., Frank, M., Lorenzen, J., Reitz, A., Brown, K., Feseker, T., Brückmann, W., 2013a. High- and low-latitude forcing of the Nile River regime during the Holocene inferred from laminated sediments of the Nile deep-sea fan. Earth Planet. Sci. Lett. 364, 98–110.
Blanchet, C.L., Frank, M., Schouten, S., 2013b. Asynchronous changes in vegetation, runoff and erosion in the Nile River watershed during the Holocene. PLoS One 9, e115958.
Bond, G., Kromer, B., Beer, J., Muscheler, R., Evans, M.N., Showers, W., Hoffmann, S., Lotti-Bond, R., Hajdas, I., Bonani, G., 2001. Persistent solar influence on North Atlantic climate during the Holocene. Science 294, 2130–2136.
Bout-Roumazeilles, V., Combourieu-Nebout, N., Desprat, S., Siani, G., Turon, J.L., Essallami, L., 2013. Tracking atmospheric and riverine terrigenous supplies variability during the last glacial and the Holocene in central Mediterranean. Clim. Past 9, 1065–1087.
Bristow, C.S., Hudson-Edwards, K.A., Chappell, A., 2010. Fertilizing the amazon and equatorial atlantic with West african dust. Geophys. Res. Lett. 37 http://dx.doi.org/10.1029/2010GL043486.
Castillo, S., Moreno, T., Querol, X., Alastuey, A., Cuevas, E., Herrmann, L., Mounkaila, M., Gibbons, W., 2008. Trace element variation in size-fractionated African desert dusts. J. Arid Environ. 72, 1034–1035.
Cheddadi, R., Nourelbait, M., Bouaissa, O., Tabel, J., Rhoujjati, A., López-Sáez, J.A., Alba-Sánchez, F., Khater, C., Ballouche, A., Dezileau, L., Lamb, H., 2015. A history of human impact on moroccan mountain landscapes. Afr. Archaeol. Rev. 32, 233–248.
Cheng, H., Sinha, A., Verheyden, S., Nader, F.H., Li, X.L., Zhang, P.Z., Yin, J.J., Yi, L., Peng, Y.B., Rao, Z.G., Ning, Y.F., Edwards, R.L., 2015. The climate variability in northern Levant over the past 20,000 years. Geophys. Res. Lett. 42, 8641–8650. http://dx.doi.org/10.1002/2015GL065397.
Chiapello, I., Moulin, C., 2002. TOMS and METEOSAT satellite records of the variability of Saharan dust transport over the Atlantic during the last two decades (1979–1997). Geophys. Res. Lett. 29, 1176. http://dx.doi.org/10.1029/2001GL013767.
Coudé-Gaussen, G., 1991. Les Poussières Sahariennes. John Libbey, Montrouge, 390 p.
Croudace, I.W., Rindby, A., Rothwell, R.G., 2006. In: ITRAX: Description and Evaluation of a New Multi-Function X-ray Core Scanner, 267. Geological Society of London Special Publication, pp. 51–63.
Cruz, J.A., Turrero, M.J., Cáceres, J.O., Marín-Roldán, A., Ortega, A.I., Garralón, A., Sánchez, L., Gómez, P., Munoz-García, M.B., Edwards, R.L., Martín-Chivelet, J., 2015. Long-term hydrological changes in northern Iberia (4.9-0.9 ky BP) from speleothem Mg/Ca ratios and cave monitoring (Ojo Guareña Karst Complex, Spain). Environ. Earth Sci. 74, 7741–7753.
deMenocal, P.B., Ortiz, J., Guilderson, T., Adkins, J., Sarnthein, M., Baker, L., Yarusinsky, M., 2000a. Abrupt onset and termination of the African Humid Period: rapid climatic responses to gradual insolation forcing. Quat. Sci. Rev. 19, 347–361.
deMenocal, P.B., Ortiz, J., Guilderson, T., Sarnthein, M., 2000b. Coherent high- and low-latitude climate variability during the Holocene warm period. Science 288, 2198–2202.
Dietze, M., Dietze, E., 2013. EMMAgeo: end-member modelling algorithm and supporting functions for grain-size analysis. R package version 0.9.0., available at: http://CRAN.R-project.org/. package=EMMAgeo.
Dietze, E., Hartmann, K., Diekmann, B., IJmker, J., Lehmkuhl, F., Opitz, S., Stauch, G., Wünnemann, B., Borchers, A., 2012. An end-member algorithm for deciphering modern detrital processes from lake sediments of Lake Donggi Cona, NE Tibetan Plateau, China. Sediment. Geol. 243-244, 169–180.
Dietze, E., Maussion, F., Ahlborn, M., Diekmann, B., Hartmann, K., Henkel, K., Kasper, T., Lockot, G., Opitz, S., Haberzettl, T., 2014. Sediment transport processes across the Tibetan Plateau inferred from robust grain-size end members in lake sediments. Clim. Past 10, 91–106.
Egerer, S., Claussen, M., Reick, C., Stanelle, T., 2016. The link between marine sediment records and changes in Holocene Saharan landscape: simulating the dust cycle. Clim. Past 12, 1009–1027.
Ehrmann, W., Schmiedl, G., Beuscher, S., Krüger, S., 2017. Intensity of african humid periods estimated from saharan dust fluxes. PLoS One 12, e0170989. http://dx.doi.org/10.1371/journal.pone.0170989.
Engelbrecht, J.P., Menéndez, I., Derbyshire, E., 2014. Sources of PM2.5 impacting on gran Canaria, Spain. Catena 117, 119–132.
Evan, A.T., Foltz, G.R., Zhang, D., Vimont, D.J., 2011. Influence of African dust on ocean atmosphere variability in the tropical Atlantic. Nat. Geosci. 4, 762–765.
Evan, A.T., Flamant, C., Gaetani, M., Guichard, F., 2016. The past, present and future of African dust. Nature 531, 493–495.
Fletcher, W.J., Debret, M., Sanchez Goñi, M.F., 2013. Mid-Holocene emergence of a low-frequency millennial oscillation in western Mediterranean climate: implications for past dynamics of the North Atlantic atmospheric westerlies. Holocene 23, 153–166.
Fletcher, W.J., Zielhofer, C., Mischke, S., Bryant, C., Xu, X., Fink, D., 2017. AMS radiocarbon dating of pollen concentrates in a karstic lake system. Quat. Geochronol. 39, 112–123.
Gasse, F., 2002. Diatom-inferred salinity and carbonate oxygen isotopes in Holocene waterbodies of the Western Sahara and Sahel (Africa). Quat. Sci. Rev. 21, 737–767.
Gasse, F., Téhet, R., Durand, A., Gibert, E., Fontes, J.-C., 1990. The arid-humid transition in the Sahara and the Sahel during the last deglaciation. Nature 346, 141–146.
Gillespie, R., Street-Perrott, F.A., Switsur, R., 1983. Post-glacial arid episodes in Ethiopia have implications for climate prediction. Nature 306, 680–683.
Ginoux, P., Prospero, J.M., Torres, O., Chin, M., 2004. Long-term simulation of global dust distribution with the GOCART model: correlation with North Atlantic Oscillation. Environ. Model. Softw. 19, 113–128.
Ginoux, P., Prospero, J.M., Gill, T.E., Hsu, N.C., Zhao, M., 2012. 2012. Global-scale attribution of anthropogenic and natural dust sources and their emission rates based on MODIS Deep Blue aerosol products. Rev. Geophys. 50, RG3005. http://dx.doi.org/10.1029/2012RG000388.
Goudie, A., 2009. Dust storms: recent developments. J. Environ. Manag. 90, 89–94.
Goudie, A.S., Middleton, N.J., 2001. Saharan dust storms: nature and consequences. Earth-Science Rev. 56, 179–204.
Goudie, A.S., Middleton, N.J., 2006. Desert Dust in the Global System. Springer, Berlin, Heidelberg, NewYork, 287 p.
Holz, C., Stuut, J.-B.W., Henrich, R., Meggers, H., 2007. Variability in terrigenous sedimentation processes off northwest Africa and its relation to climate changes: inferences from grain-size distributions of a Holocene marine sediment record. Sediment. Geol. 202, 499–508.
Jaramillo-Vélez, A., Menéndez, I., Alonso, I., Mangas, J., Hernández-León, S., 2016. Grain size, morphometry and mineralogy of airborne input in the Canary basin: evidence of iron particle retention in the mixed layer. Sci. Mar. 80, 395–408.
Jiang, H., Muscheler, R., Björck, S., Seidenkrantz, M.S., Olsen, J., Sha, L., Sjolte, J., Eiríksson, J., Ran, L., Knudsen, K.L., Knudsen, M., 2015. Solar forcing of Holocene summer sea-surface temperatures in the northern North Atlantic. Geology 43, 203–206.
Jickells, T.D., An, Z.S., Andersen, K.K., Baker, A.R., Bergametti, G., Brooks, N., Cao, J.J., Boyd, P.W., Duce, R.A., Hunter, K.A., Kawahata, H., Kubilay, N., laRoche, J., Liss, P.S., Mahowald, N., Prospero, J.M., Ridgwell, A.J., Tegen, I., Torres, R., 2005. Global iron connections between desert dust, ocean biogeochemistry, and climate. Science 308, 67–71.
Jiménez-Espejo, F.J., García-Alix, A., Jiménez-Moreno, G., Rodrigo-Gámiz, M., Anderson, R.S., Rodríguez-Tovar, F.J., Martínez-Ruiz, F., Giralt, S., Delgado Huertas, A., Pardo-Igúzquiza, E., 2014. Saharan aeolian input and effective humidity variations over western Europe during the Holocene from a high altitude record. Chem. Geol. 374-375, 1–12.
Jullien, E., Grousset, F., Malaizé, B., Duprat, J., Sanchez-Goni, M.F., Eynaud, F., Charlier, K., Schneider, R., Bory, A., Bout, V., Flores, J.A., 2007. Low-latitude "dusty events" vs. high-latitude "icy Heinrich events". Quat. Res. 68, 379–386.
Kaiser, H.F., 1958. The varimax criterion for analytic rotation in factor analysis. Psychometrika 23, 187–200.
Kandler, K., Schütz, L., Deutscher, C., Ebert, M., Hofmann, H., Jäckel, S., Jaenicke, R., Knippertz, P., Lieke, K., Massling, A., Petzold, A., Schladitz, A., Weinzierl, B., Wiedensohler, A., Zorn, S., Weinbruch, S., 2009. Size distribution, mass concentration, chemical and mineralogical composition and derived optical parameters of the boundary layer aerosol at Tinfou, Morocco, during SARUM 2006. Tellus 61B, 32–50.
Kaufman, Y.J., Tanre, D., Boucher, O., 2002. A satellite view of aerosols in the climate system. Nature 419, 215–223.
Kröpelin, S., Verschuren, D., Lézine, A.-M., Eggermont, H., Cocquyt, C., Francus, P., Cazet, J.-P., Fagot, M., Rumes, B., Russell, M., Darius, F., Conley, D.J., Schuster, M., von Suchodoletz, H., Engstrom, D.R., 2008. Climate-Driven ecosystem succession in the Sahara: the past 6000 years. Science 320, 765–768.
Kuhlmann, H., Meggers, H., Freudenthal, T., Wefer, G., 2004. The transition of the monsoonal and the N Atlantic climate system off NW Africa during the Holocene. Geophys. Res. Lett. 31, L22204. http://dx.doi.org/10.1029/2004GL021267.
Kuper, R., Kröpelin, S., 2006. Climate-controlled Holocene occupation in the Sahara: motor of Africa's evolution. Science 303, 803–807.
Kylander, M.E., Ampel, L., Wohlfarth, B., Veres, D., 2011. High-resolution X-ray fluorescence core scanning analysis of Les Echets (France) sedimentary sequence: new insights from chemical proxies. J. Quat. Sci. 26, 109–117.
Le Roux, G., Fagel, N., De Vleeschouwer, F., Krachler, M., Debaille, V., Stille, P., Mattielli, N., van der Knaap, W.O., van Leeuwen, J.F.N., Shotyk, W., 2012. Volcano- and climate-driven changes in atmospheric dust sources and fluxes since the Late Glacial in Central Europe. Geology 40, 335–338.
Liu, Z., Wang, Y., Gallimore, R., Gasse, F., Johnson, T., deMenocal, P., Adkins, J., Notaro, M., Prentice, I.C., Kutzbach, J., Jacob, R., Behling, P., Wang, L., Ong, E., 2007. Simulating the transient evolution and abrupt change of Northern Africa atmosphere–ocean–terrestrial ecosystem in the Holocene. Quat. Sci. Rev. 26, 1818–1837.
Longman, J., Veres, D., Ersek, V., Salzmann, U., Hubay, K., Bormann, M., Wennrich, V., Schäbitz, F., 2017. Periodic input of dust over the Eastern Carpathians during the Holocene linked with Saharan desertification and human impact. Clim. Past Discuss. http://dx.doi.org/10.5194/cp-2017-6, 2017.
Mahowald, N., Luo, C., del Corral, J., Zender, C.S., 2003. Interannual variability in atmospheric mineral aerosols from a 22-year model simulation and observational data. J. Geophys. Res. 108, 4352. http://dx.doi.org/10.1029/2002JD002821.
Mahowald, N.M., Kloster, S., Engelstaedter, S., Moore, J.K., Mukhopadhyay, S., McConnell, J.R., Albani, S., Doney, S.C., Bhattacharya, A., Curran, M.A.J., Flanner, M.G., Hoffman, F.M., Lawrence, D.M., Lindsay, K., Mayewski, P.A., Neff, J., Rothenberg, D., Thomas, E., Thornton, P.E., Zender, C.S., 2010. Observed 20th century desert dust variability: impact on climate and biogeochemistry. Atmospheric Chem. Phys. 10, 10875–10893.
Manning, K., Timpson, A., 2014. The demographic response to Holocene climate change in the Sahara. Quat. Sci. Rev. 101, 28–35.

Margaritelli, G., Vallefuoco, M., Di Rita, F., Capotondi, L., Bellucci, L.G., Insinga, D.D., Petrosino, P., Bonomo, S., Cachof, I., Cascella, A., Ferraroa, L., Florindo, F., Lubritto, C., Lurcock, P.C., Magri, D., Pelosi, N., Rettori, R., Lirer, F., 2016. Marine response to climate changes during the last five millennia in the central Mediterranean Sea. Glob. Planet. Change 142, 53–72.

Menéndez, I., Díaz-Hernández, J.L., Mangas, J., Alonso, I., Sánchez-Soto, P.J., 2007. Airborne dust accumulation and soil development in the north-East sector of gran Canaria (canary islands, Spain). J. Environ. 71, 57–81.

Moreno, A., Cacho, I., Canals, M., Prins, M.A., Sánchez-Goñi, M.-F., Grimalt, J.O., 2002. Saharan dust transport and high-latitude glacial climatic variability: the alboran sea record. Quat. Res. 58, 318–328.

Moreno, T., Querol, X., Castillo, S., Alastuey, A., Cuevas, E., Herrmann, L., Mounkaila, M., Elvira, J., Gibbons, W., 2006. Geochemical variations in aeolian mineral particles from the Sahara-Sahel dust corridor. Chemosphere 65, 261–270.

Moulin, C., Lambert, C.E., Dulac, F., Dayan, U., 1997. Control of atmospheric export of dust from north Africa by the north atlantic oscillation. Nature 387, 691–694.

Muhs, D.R., Bush, C.A., Stewart, K.C., 1990. Geochemical evidence of Saharan dust parent material for soils developed on Quaternary limestones of Caribbean and Western Atlantic islands. Quat. Res. 33, 157–177.

NASA, 2016. MODIS composite image obtained on 26th June 2012 [27th December 2016]. https://worldview.earthdata.nasa.gov.

Piqué, A., 2001. Geology of Northwest Africa. I-XIV. Gebrüder Borntraeger, Berlin, Stuttgart, 310 p.

Prospero, J.M., Lamb, P.J., 2003. African droughts and dust transport to the Caribbean: climate change implications. Science 302, 1024–1027.

Renssen, H., Brovkin, V., Fichefet, T., Goosse, H., 2006. Simulation of the Holocene climate evolution in northern Africa: the termination of the african humid period. Quat. Int. 150, 95–102.

Rodrigo-Gámiz, M., Martínez-Ruiz, F., Rodríguez-Tovar, F.J., Jiménez-Espejo, F.J., Eulogio Pardo-Igúzquiza, E., 2014. Millennial- to centennial-scale climate periodicities and forcing mechanisms in the westernmost Mediterranean for the past 20,000 yr. Quat. Res. 81, 78–93.

Rossignol-Strick, M., Nesteroff, W., Olive, P., Vergnaud-Grazzini, C., 1982. After the deluge: Mediterranean stagnation and sapropel formation. Nature 295, 105–110.

Ryder, C.L., Highwood, E.J., Rosenberg, P.D., Trembath, J., Brooke, J.K., Bart, M., Dean, A., Crosier, J., Dorsey, J., Brindley, H., Banks, J., Marsham, J.H., McQuaid, J.B., Sodemann, H., Washington, R., 2013a. Optical properties of Saharan dust aerosol and contribution from the coarse mode as measured during the Fennec 2011 aircraft campaign. Atmos. Chem. Phys. 13, 303–325.

Ryder, C.L., Highwood, E.J., Lai, T.M., Sodemann, H., Marsham, J.H., 2013b. Impact of atmospheric transport on the evolution of microphysical and optical properties of Saharan dust. Geophys. Res. Lett. 40 http://dx.doi.org/10.1002/grl.50482.

Saadi, M., Hilali, E.A., Bensaïd, M., Boudda, A., Dahmani, M., 1985. Carte Géologique du Maroc 1/1,000,000. Notes et Mémoires 260. Editions du Service Géologique du Maroc, Rabat.

Sayad, A., Chakiri, S., Martin, C., Bejjaji, Z., Echarfaoui, H., 2011. Effet des conditions climatiques sur le niveau du lac Sidi Ali (Moyen Atlas, Maroc). Physio-Géo 5, 251–268.

Schepanski, K., Tegen, I., Todd, M.C., Heinold, B., Bönisch, G., Laurent, B., Macke, A., 2009. Meteorological processes forcing Saharan dust emission inferred from MSG-SEVIRI observations of subdaily dust source activation and numerical models. J. Geophys. Res. 114, D10201.

Schepanski, K., Mallet, M., Heinold, B., Ulrich, M., 2016. North African dust transport toward the western Mediterranean basin: atmospheric controls on dust source activation and transport pathways during June-July 2013. Atmos. Chem. Phys. http://dx.doi.org/10.5194/acp-16-1-2016.

Scheuvens, D., Schütz, L., Kandler, K., Ebert, M., Weinbruch, S., 2013. Bulk composition of northern African dust and its source sediments – a compilation. Earth-Science Rev. 116, 170–194.

Schlüter, T., 2008. Geological Atlas of Africa. Springer, Berlin.

Schmiedl, G., Kuhnt, T., Ehrmann, W., Emeis, K.-C., Hamann, Y., Kotthoff, U., Dulski, P., Pross, J., 2010. Climatic forcing of eastern Mediterranean deep-water formation and benthic ecosystems during the past 22 000 years. Quat. Sci. Rev. 29, 3006–3020.

Shanahan, T.M., McKay, N.P., Hughen, K.A., Overpeck, J.T., Otto-Bliesner, B., Heil, C.W., King, J., Scholz, C.A., Peck, J., 2015. The time-transgressive termination of the african humid period. Nat. Geosci. 8, 140–144.

Staubwasser, M., Sirocko, F., Grootes, P.M., Segl, M., 2003. Climate change at the 4.2 ka BP termination of the Indus valley civilization and Holocene south Asian monsoon variability. Geophys. Res. Lett. 30, 1425. http://dx.doi.org/10.1029/2002GL016822.

Suchodoletz, H. von, Glaser, B., Thrippleton, T., Broder, T., Zang, U., Eigenmann, R., Kopp, B., Reichert, M., Zöller, L., 2013. Saharan dust deposits on La palma (canary islands, Spain). Catena 103, 44–52.

Stuut, J.B., Smalley, I., O'Hara-Dhand, K., 2009. Aeolian dust in Europe: african sources and european deposits. Quat. Int. 198, 234–245.

Sun, D., Bloemendal, J., Rea, D.K., An, Z., Vandenberghe, J., Lu, H., Su, R., Liu, T., 2004. Bimodal grain-size distribution of Chinese loess, and its palaeoclimatic implications. Catena 55, 325–340.

Swezey, C., 2001. Eolian sediment responses to late Quaternary climate changes: temporal and spatial patterns in the Sahara. Palaeogeogr. Palaeoclimatol. Palaeoecol. 167, 119–155.

Tierney, J.E., deMenocal, P.B., 2013. Abrupt shifts in horn of Africa hydroclimate since the last glacial maximum. Science 342, 843–846.

Tierney, J.E., Pausata, F.S.R., deMenocal, P.B., 2017. Rainfall regimes of the green Sahara. Sci. Adv. 3, e1601503.

Thompson, L.G., Mosley-Thompson, E., Davis, M.E., Henderson, K.A., Brecher, H.H., Zagorodnov, V.S., Mashiotta, T.A., Lin, P.N., Mikhalenko, V.N., Hardy, D.R., Beer, J., 2002. Kilimanjaro ice core records: evidence of Holocene climate change in tropical Africa. Science 298, 589–593.

Tjallingii, R., Claussen, M., Stuut, J.B.W., Fohlmeister, J., Jahn, A., Bickert, T., Lamy, F., Röhl, U., 2008. Coherent high- and low-latitude control the northwest African hydrological balance. Nat. Geosci. 1, 670–675.

Torres-Padrón, M.E., Gelado-Caballero, M.D., Collado-Sánchez, C., Siruela-Matos, V.F., Cardona-Castellano, P.J., Hernández-Brito, J.J., 2002. Variability of dust inputs to the CANIGO zone. Deep-Sea Res. II 49, 3455–3464.

Vandenberghe, J., 2013. Grain size of fine-grained windblown sediment: a powerful proxy for process identification. Earth-Science Rev. 121, 18–30.

Wanner, H., Mercolli, L., Grosjean, M., Ritz, S.P., 2015. Holocene climate variability and change; a data-based review. J. Geol. Soc. Lond. 172, 254–263.

Wassenburg, J.A., Dietrich, S., Fietzke, J., Fohlmeister, J., Jochum, K.P., Scholz, D., Richter, D.K., Sabaoui, A., Spötl, C., Lohmann, G., Andreae, M.O., Immenhauser, A., 2016. Reorganization of the north atlantic oscillation during early Holocene deglaciation. Nat. Geosci. 9, 602–607.

Wehausen, R., Brumsack, H.J., 2000. Chemical cycles in Pliocene sapropel-bearing and sapropel-barren eastern Mediterranean sediments. Palaeogeogr. Palaeoclimatol. Palaeoecol. 158, 325–352.

Weltje, G.J., Bloemsma, M.R., Tjallingii, R., Heslop, D., Röhl, U., Croudace, I.W., 2015. Prediction of geochemical composition from XRF core scanner data: a new multivariate approach including automatic selection of calibration samples and quantification of uncertainties. In: Croudace, I.W., Rothwell, R.G. (Eds.), Micro-XRF Studies of Sediment Cores, Developments in Palaeoenvironmental Research. Springer, Berlin Heidelberg, pp. 507–534.

Westphal, D.L., Toon, O.B., Carlson, T.N., 1988. A case study of mobilization and transport of Saharan dust. J. Atmos. Sci. 45, 2145–2175.

Weiss, H., 2016. Global megadrought, societal collapse and resilience at 4.2-3.9 ka BP across the Mediterranean and west Asia. Pages Mag. 24, 62–63.

Williams, R.H., McGee, D., Kinsley, C.W., Ridley, D.A., Hu, S., Fedorov, A., Tal, I., Murray, R.W., deMenocal, P.B., 2016. Glacial to Holocene changes in trans-Atlantic Saharan dust transport and dust-climate feedbacks. Sci. Adv. 2, e1600445.

Wu, J., Böning, P., Pahnke, K., Tachikawa, K., de Lange, G.J., 2016. Unraveling North-African riverine and eolian contributions to central Mediterranean sediments during Holocene sapropel S1 formation. Quat. Sci. Rev. 152, 31–48.

Zielhofer, C., Fletcher, W.J., Mischke, S., De Batist, M., Campbell, J.F.E., Joannin, S., Tjallingii, R., El Hamouti, N., Junginger, A., Stele, A., Bussmann, J., Schneider, B., Lauer, T., Spitzer, K., Strumpler, M., Brachert, T., Mikdad, A., 2017. Atlantic forcing and Western Mediterranean winter rain minima during the last 12,000 years. Quat. Sci. Rev. 157, 29–51.